RSC Advances

ROYAL SOCIETY OF CHEMISTRY

www.rsc.org/advances

Structural, optical and photoconductivity characteristics of pristine $FeO.Fe_2O_3$ and NTPI-$FeO.Fe_2O_3$ nanocomposite : Aggregation induced emission enhancement of fluorescent organic nanoprobe of thiophene appended phenanthrimidazole derivative

Jayaraman Jayabharathi*, Annadurai Prabhakaran, Chockalingam Karunakaran, Venugopal Thanikachalam, Munusamy Sundharesan

Department of Chemistry, Annamalai University, Annamalainagar 608 002, Tamilnadu, India

* Address for correspondence

Dr. J. Jayabharathi
Professor of Chemistry
Department of Chemistry
Annamalai University
Annamalainagar 608 002
Tamilnadu, India.
Tel: +91 9443940735
E-mail: jtchalam2005@yahoo.

* Corresponding author. Tel.: +91 9443940735
E-mail address: jtchalam2005@yahoo.co.in

Abstract

In this manuscript we report the successful synthesis of pristine $FeO.Fe_2O_3$, 1-(naphthalen-1-yl)-2-(thiophen-2-yl)-1H-phenanthro[9,10-d]imidazole(NTPI), fluoresecnt organic nanoparticles (FONs) of NTPI and NTPI-FeO.Fe2O3 nanocomposite. Pristine $FeO.Fe_2O_3$ and NTPI- $FeO.Fe_2O_3$ nanocomposite were characterised by XRD, SEM, EDS, TEM, SAED, XPS, DLS, UV, PL, life time FT-IR and magnetic hysteresis. We have extensively studied the photoluminescence and photoconductivity of both pristine $FeO.Fe_2O_3$ and NTPI- $FeO.Fe_2O_3$ nanocomposite. An enhancement in photoluminescence (PL) emission and reduced photoconductivity is observed for NTPI- $FeO.Fe_2O_3$ nanocomposite when compared to bare $FeO.Fe_2O_3$. NTPI adsorption on $FeO.Fe_2O_3$ reduces the non-radiative trap levels at the interface, resulting enhancement of PL intensity of nanocomposite. For $FeO.Fe_2O_3$, exponential rise and decay in photocurrent is observed upon UV irradiation in the ON and OFF state, respectively and unusual behavior of photocurrent is observed for NTPI- $FeO.Fe_2O_3$composite. The NTPI behave as AIEE-active chemosensor for the detection of ferric ions in aqueous solution. Theoretical investigation shows that the binding energy and energy gap of the imidazole composites are highly dependent on the nature of the iron oxide cluster and the existence of charge transfer in the imidazole–iron oxide composite is explained.

Keywords: DLS; XPS; NTPI- $FeO.Fe_2O_3$composites; photo-current; NTPI-FeO clusters; nanoaggregation; UV - ON and OFF state.

1. Introduction

FeO.Fe2O3 nanoparticles have been the subject of intense interest because of their potential applications in several advanced technological areas due to their fundamental properties and potential applications in medical diagnosis and therapy, drug delivery, magnetic resonance imaging and cancer hypothermia treatment [1-7]. The magnetic ions in solid materials are arranged in a periodic lattice and their magnetic moments collectively interact through molecular

exchange fields and give rise to a long-range magnetic ordering. Among all iron oxide nanoparticles, FeO.Fe2O3 exhibits unique properties due to the presence of iron cations in two valence states on tetrahedral and octahedral sites with an inverse pristine spinel structure. Several groups have investigated the photoconductivity of silica based nanocomposite systems [8–11]. Enhanced photoconductivity (PC) has also been observed for SiO_2 based ZnO nanocomposites, and a reduced photoconductivity was reported for ZnO quantum dots embedded in a SiO_2 matrix. The PC study depends exclusively on the surface properties of the nanomaterials. Various explanations have been proposed to explain the PC of different oxide materials [12–14]. Broadly, two different mechanisms have been proposed for the origin of PC, (i) fast band to band transition with characteristic time in the nanosecond range and (ii) the adsorption/ desorption of oxygen molecules at the interfaces of the nanomaterials.

Cell labeling strategies find application of superparamagnetic ferrite either through conjugating the magnetic nanoparticles to the cellular surface of the stem cell or by internalization of the particles into the cell. With recent developments in nanotechnology, fluorescent organic nanoparticles (FONs) with aggregation-induced enhanced emission (AIEE) gained increasing attention because of their diverse molecular structure, low toxicity and good stability in aqueous solution [15]. These AIEE-active FONs overcome the fluorescence quenching of conventional organic dyes in water, equipping bio/chemo-sensors with a new design strategy. The fascinating optical properties make them as fluorescent probes for various biological detection and *in vivo* bioimaging [16]. It is envisaged that AIEE nanosensors are sensitive and less cytotoxic than their inorganic counterparts [17] and used to sense and detect protein [18], DNA [19], carbon dioxide gas [20] and D-glucose [21]. FON probes are used for detecting metal ions [22], namely, Hg^{2+} [23], Cu^{2+} [24] and Ag^{+} [25]. FONs of pentacenequinine

derivative are used to detect Fe^{3+} in a mixed aqueous solution with a detection limit of 100 nM. However, this Fe^{3+} sensor exhibits strong fluorescence quenching when bound with Fe^{3+} because of the paramagnetic nature of iron. Since emission quenching has significant problem in practical applications, development of new biocompatible fluorescent probes for Fe^{3+} detection in aqueous media, with selective Fe^{3+} amplified emission, remains a challenge.

In this work, synthesis and characterization of pristine nano $FeO.Fe_2O_3$and $FeO.Fe_2O_3$-NTPI nanocomposite are reported. The unusual optical properties of $FeO.Fe_2O_3$-NTPI nanocomposite, *i.e.,* enhancement in PL and reduction in PC, have been analysed in detail. We have synthesized a novel NTPI derivative that can form highly fluorescent organic nanoparticles (NTPI FONs) with AIEE characteristics in aqueous media, providing a new approach for selective turn-on fluorescence detection of Fe^{3+} ion with detection sensitivity up to the picogram level. The charge transfer interaction of naphthyl thiophene phenanthrimidazole with iron oxide clusters has been analysed in detail.

2. Materials and methods

2.1. Materials and measurements

Phenanthroquinone, thiophene-2-carbaldehyde, naphthylamine and all other reagents have been purchased from Sigma-Aldrich. The ultraviolet-visible (UV-vis) spectra were obtained with Perkin Elmer Lambda 35 UV-vis spectrophotometer and corrected for background absorption due to solvent. The photoluminescence (PL) spectra were recorded on a PerkinElmer LS55 fluorescence spectrometer. NMR spectra were recorded on Bruker 400 MHz NMR spectrometer. The mass spectra of the samples were obtained using an Agilent LCMS VL SD in electron ionization mode. Cyclic voltammetric (CV) analyses were performed by using CHI 630A potentiostat electrochemical analyzer. Fluorescence lifetime measurements were carried out with

a nanosecond time correlated single photon counting (TCSPC) spectrometer Horiba Fluorocube-01-NL lifetime system with nano LED (pulsed diode excitation source) as the excitation source and TBX-PS as detector. The absolute quantum yields were measured by comparing fluorescence intensities (integrated areas) of a standard sample (coumarin). The high -resolution scanning electron micrographs (HR-SEM) were obtained with a FEI Quanta FEG in high -vacuum mode. The transmission electron microscopic (TEM) images at high resolution were recorded with a TEM using 200 kV electron beam. Energy dispersive X-ray spectral (EDS) analysis was also made with a FEI Quanta FEG. The selected area electron diffraction (SAED) patterns were obtained using a Philips TEM equipped with CCD camera at an acceleration voltage of 200 kV. The sample was dispersed in ethanol by sonication and deposited on carbon-coated copper grid. The powder X-ray diffractograms (XRD) were obtained in a 2θ range of 10−80° employing a Eqinox 1000 diffractometer using Cu Kα rays at 1.5406 Å with a tube current of 30 mA at 40 kV. The instrument Perkin-Elmer Lambda 35 with RSA-PE-20 integrating sphere attachment was used to record the UV-visible diffuse reflectance spectrum (DRS). The specific surface area of the samples was determined through nitrogen adsorption at 77 K on the basis of the Brunauer–Emmett–Teller (BET) equation using a Micromeritics ASAP 2020 V3.00 H. Photoconductivity measurements were carried out by two-probe technique at room temperature. Ohmic contact properties were checked by measuring the current–voltage characteristics. A light source of variable intensity (tungsten lamp, 100 W) was used to illuminate the sample. An lx meter (Lutron LX-101) was used for the measurement of the intensity of the incident light. In order to study the photoconductivity with white unpolarised radiation, the sample was illuminated at normal incidence to the surface plane. The illumination intensity was varied in magnitude from 600 to 3000 lx. For the measurement of dark

conductivity the crystal was kept in a dark chamber for 15 min. Gold electrodes were used and the photoconductance was calculated using the geometrical data of the samples. Transient photoconductivity measurements were carried out on these single crystals at a fixed light intensity of 3000 lx. The single crystal was exposed to light radiation and current was recorded simultaneously for a given period and the light was switched off and a current decay was followed. Theoretical calculations were performed using density functional theory (DFT) as implemented with Gaussian-03 program using the Becke3-Lee-Yang-Parr (B3LYP) functional supplemented with the standard 6-31G (d, p) basis set [26].

2.2. Synthesis of 1-(naphthalen-1-yl)-2-(thiophen-2-yl)-1H-phenanthro[9,10-d]imidazole(NTPI)

A mixture of phenanthriquinone (1 mmol), thiophene-2-carbaldehyde (1 mmol), 1-naphthylamine (1 mmol), ammonium acetate (1 mmol) and indium trifluoride (InF_3, 1 mol %) was stirred at 80 °C. The progress of the reaction was monitored by TLC. After completion of the reaction, the mixture was cooled, dissolved in acetone and filtered. The product was purified by column chromatography using benzene: ethyl acetate (9:1) as the eluent [27]. M.p.245ºC. Anal. calcd. for $C_{29}H_{18}N_2S$: C, 81.66; H, 4.25; N, 6.57. Found: C, 81.64; H, 4.23; N 6.54. ^{1}H NMR (400 MHz, DMSO): δ 7.28 (q, 2H), 7.68 (M, 8H), 7.93 (d, *J=8.0 Hz,* 2H), 8.49 (dd, *J=8.4 & 3.4 Hz,* 3H), 8.73 (q, 3H). ^{13}C NMR (100 MHz, DMSO): δ 121.82, 123.70, 124.10, 125.43, 125.83, 126.60, 127.16, 127.49, 127.82, 128.24, 133.75, 136.64, 144.90. MS: m/z. 426.12 [M+].

2.3. Fabrication of FONs of NTPI

Fluoresecnt organic nanoparticles (FONs) of NTPI were prepared by re-precipitation method. About 1mL of NTPI (0.1-0.3 mM in THF) was injected into 100 mL double distilled water. The solutions were sonicated to ensure rapid mixing. The formed FONs were characterised with SEM, TEM and DLS.

2.4. Sol-gel synthesis of magnetite $FeO.Fe_2O_3$

Ferric nitrate and ethylene glycol were dissolved in proper ratios and was stirred for 2 h at 400 °C. Then, the prepared sol was heated to 800 °C to get brown gel. The formed glassy like brown gel was allowed to age overnight. The gel was aged at room temperature for about 1 h and then annealed at 200, 300 and 400 °C in furnace under air atmosphere.

2.5. Sol-gel synthesis of $FeO.Fe_2O_3$*– NTPI composite*

About 1 mmol of NTPI in dimethyl sulphoxide was added to 1 mmol of Fe_3O_4 nanoparticles suspended in dimethyl sulphoxide under constant stirring for 3 h. The solid was filtered, washed with dimethyl sulphoxide and dried at 110 ºC.

3. Results and discussion

3.1. Crystalline structure and Morphology

The crystallographic phases of both pristine $FeO.Fe_2O_3$ and $FeO.Fe_2O_3$–NTPI nanocomposite were identified by X-ray diffraction, as shown in Figure 1. The pattern shows the presence of rhombohedral Fe_2O_3 and tetragonal FeO. The diffraction peaks at 33.27, 39.80, 49.52, 57.40, 62.06, 74.69 and 79.65° correspond to 104, 006, 024, 122, 214, 217 and 131 planes of rhombohedral Fe_2O_3 [28,29]. The observed diffraction pattern is in well-agreement with the standard JCPDS 89-8104. The mean crystallite size (L) of the synthesized $FeO.Fe_2O_3$is 18 nm and the calculated surface area is 57.6 m^2/g. The peak at 35.93° corresponds to (313) plane of tetragonal FeO (JCPDS 89-5894). The recorded XRD of $FeO.Fe_2O_3$–NTPI nanocomposite is in agreement with JCPDS 89-8104 (rhombohedral Fe_2O_3) & JCPDS 89-5894(tetragonal FeO) (Figure 1). The diffraction peaks at 33.56, 39.97, 49.83, 57.53, 62.63, 74.32 and 79.46° correspond to 104, 006, 024, 122, 214, 217 and 131 planes, respectively, of Fe_2O_3. The mean crystallite size (L) of the $FeO.Fe_2O_3$–NTPI composite is 41.3 nm and the calculated surface area

is 25.6 m^2/g. The peak at 35.32° corresponds to (313) plane of tetragonal FeO. The small hump at 53.4° is likely due to the adsorption of NTPI on $FeO.Fe_2O_3$. All the peaks in the recorded XRD pattern are identified. The absence of any other unassigned peak indicates the purity of the synthesized crystalline $FeO.Fe_2O_3$and $FeO.Fe_2O_3$-NTPI synthesized. Hence, it can be concluded that the NTPI adsorption on $FeO.Fe_2O_3$has not changed the crystal structure of the $FeO.Fe_2O_3$ particles. The TEM images of pristine $FeO.Fe_2O_3$ and $FeO.Fe_2O_3$–NTPI nanocomposite are shown in Figures 2 & 3. They confirm the synthesized materials as nanoparticles. The average particle sizes measured in the TEM is larger than the average crystalline size deduced from the XRD results. This indicates that the nanoparticles associate among themselves. SAED pattern of pristine $FeO.Fe_2O_3$ (Figure 2d) and $FeO.Fe_2O_3$-NTPI (Figure 3d) reveal diffraction rings with bright spots and one indexed to 104, 006, 024, 122, 214, 217 and 131 planes of rhombohedral Fe_2O_3 and 313 plane of tetragonal FeO.

The SEM images of pristine $FeO.Fe_2O_3$and $FeO.Fe_2O_3$-NTPI nanocomposite are shown in Figure 4. SEM image of $FeO.Fe_2O_3$-NTPI reveal agglomeration of the nanoparticles. The EDS of pristine $FeO.Fe_2O_3$and $FeO.Fe_2O_3$–NTPI composite are shown in Figure 5. EDS of pristine $FeO.Fe_2O_3$ reveals the presence of iron and oxygen which is in agreement with the formation of $FeO.Fe_2O_3$nanoparticles and a typical optical absorption peak observed at 0.5 keV is likely due to surface Plasmon resonance. Figure 5 displays the presence of carbon, oxygen, sulphur and nitrogen along with iron in the composite. This shows the binding of NTPI with FeO.Fe2O3 nanoparticles. The BET surface and pore volume of bare $FeO.Fe_2O_3$ and $FeO.Fe_2O_3$-NTPI nanocomposite are given in Table 1. The BET surface area of $FeO.Fe_2O_3$-NTPI nanocomposite (32.82 m^2g^{-1}) is larger than that of bare $FeO.Fe_2O_3$ (23.10 $m^2\ g^{-1}$).

3.2. Dynamic light scattering (DLS) studies & X-ray photoelectron spectroscopy

The DLS images presented in Figure 6 show the average sizes of the synthesized pristine nano $FeO.Fe_2O_3$and $FeO.Fe_2O_3$-NTPInanocomposite as 18 and 41 nm, respectively. The DLS results confirmed the size of the particles obtained from XRD and TEM experiments. The negative ζ potential [$FeO.Fe_2O_3$- (-48.4 mV) and $FeO.Fe_2O_3$-NTPI (-8.5 mV)] indicates the strong repellent forces between particles due to high electrical charge on the surface of pristine $FeO.Fe_2O_3$and $FeO.Fe_2O_3$- NTPI composite, which in turn results in high stability. The surface chemical composition and chemical states of $FeO.Fe_2O_3$ and $FeO.Fe_2O_3$-NTPI were investigated by XPS (Figure 7). In the spectra of $FeO.Fe_2O_3$, the peaks observed at 709 and 723 eV are the characteristic doublets of Fe $2P_{3/2}$ and Fe $2P_{1/2}$, respectively (FeO) and at 711 and 724 eV are the characteristic doublets of Fe $2P_{3/2}$ and Fe $2P_{1/2}$, respectively (Fe_2O_3). The O1S peak appears at 529.6 eV. In the spectra of NTPI- $FeO.Fe_2O_3$composite, the peaks observed at 710 and 712 eV are the characteristic doublets of Fe $2P_{3/2}$ and Fe $2P_{1/2}$, respectively (FeO) and at 723.5 and 725 eV are the characteristic doublets of Fe $2P_{3/2}$ and Fe $2P_{1/2}$, respectively (Fe_2O_3). The N1S, O1S and S2P peak appears at 400, 529.6 and 163 eV, respectively. The shifting of Fe $P_{3/2}$ and Fe $p_{1/2}$ of both FeO and Fe_2O_3 and O1S peaks confirm the formation of $FeO.Fe_2O_3$-NTPI composite.

3.3. Band gap and emission

The diffuse reflectance spectra (DRS) of the synthesized pristine $FeO.Fe_2O_3$, NTPI and $FeO.Fe_2O_3$-NTPI nanoparticles are presented in Figure 8. The synthesized nano $FeO.Fe_2O_3$, NTPI and $FeO.Fe_2O_3$-NTPI composite display broad absorption bands around 298, 342 and 338 nm respectively. The reflectance data are reported as *F(R)* values, obtained by the application of the Kubelka–Munk algorithm [$F(R) = (1 - R)^2/2R$]. The figure shows that complexation shifts the absorption edge to visible region. Plots of (i) $[F(R)h\nu]^2$ and (ii) $[F(R)h\nu]^{1/2}$ versus photon energy

provide the (i) direct and (ii) indirect band gaps of the synthesized pristine $FeO.Fe_2O_3$, NTPI and $FeO.Fe_2O_3$-NTPI nanocomposite as (i) 3.13, 3.03 and 2.93 eV and (ii) 3.02, 2.82 and 2.54 eV, respectively. These values show that complexation decreases the band gap. Photoluminescence excitation curves for $FeO.Fe_2O_3$, NTPI and $FeO.Fe_2O_3$-NTPI are shown in Figure 9a. Both the samples show a pronounced absorption peak between 305–400 nm, which is in agreement with the earlier report [30]. The peak position ~327 nm (FeO.Fe2O3), 330 nm (NTPI) and 332 nm ($FeO.Fe_2O_3$-NTPI) was attributed to the band edge excitation of the samples. In addition, there is slight peak shift in the spectra for the $FeO.Fe_2O_3$-NTPI composite and there is decrease in the band gap. However, the sharper absorption edge at 332 nm for $FeO.Fe_2O_3$-NTPI composite when compared to pristine $FeO.Fe_2O_3$gives indication of the modified surface properties of pristine $FeO.Fe_2O_3$ after bonding with NTPI.

The PL emission peaks for pristine $FeO.Fe_2O_3$, NTPI and $FeO.Fe_2O_3$-NTPI composite are shown in Figure 9b, FeO.Fe2O3 emits at 419 nm, NTPI at 429 nm and $FeO.Fe_2O_3$-NTPI composite at 412 nm. The broad emission peak is observed for $FeO.Fe_2O_3$ because of oxygen vacancies, which play a key role in the origin of violet emission and is similar to the green PL observed for Zn [31-33]. The $FeO.Fe_2O_3$ nanoparticles have a very large surface area and thereby have a large number of dangling bonds associated with the oxygen vacancies, which constitutes their surface defects. These defects form donor states below the conduction band (CB). The PL emission arises from the recombination of electrons in the donor states with photoexcited holes in the valence band (VB). Furthermore, the $FeO.Fe_2O_3$ show broadening in their PL emission with reduced intensity, which is a result of the scattering of incident and emitted photons from the highly roughened surface of $FeO.Fe_2O_3$. When the light scattering is stronger than absorption, the efficiency of the electron transfer from NTPI to semiconductor becomes high. Thus, the UV-

light emission intensity of the composite nanocrystals becomes much higher than that of the $FeO.Fe_2O_3$. However, the interfacial region seems to supply routes for the effective electron transfer from ligand to $FeO.Fe_2O_3$since the emission intensity dominantly increases in $FeO.Fe_2O_3$-NTPI compared to pristine $FeO.Fe_2O_3$.

3.4. Magnetic behaviour

Magnetic hysteresis curves recorded at room temperature for pristine $FeO.Fe_2O_3$nanocrystals and FeO.Fe2O3-NTPI nanocomposite are presented in Figure 10a. Magnetic properties like saturation magnetization (M_S), coercivity (H_C) and remanence magnetization (M_R) have been evaluated [34]. The hysteresis loops of $FeO.Fe_2O_3$ and $FeO.Fe_2O_3$-NTPI composite are of normal S-shape, and the thickness of the loop reflects the coercivity of the material. Precursor $FeO.Fe_2O_3$ nanocrystals and $FeO.Fe_2O_3$-NTPI nanocomposite are superparamagnetic. The hysteresis loops show that the coercivities of $FeO.Fe_2O_3$-NTPI nanocomposite are too small. The HC of $FeO.Fe_2O_3$ nanocrystals and $FeO.Fe_2O_3$ -NTPI nanocomposite are 39 and 47 Oe, respectively. The coercivity of precursor $FeO.Fe_2O_3$ nanoparticles is comparable to that of $FeO.Fe_2O_3$ microspheres (37 Oe) [35] and is smaller than those of $FeO.Fe_2O_3$ microoctahedra obtained by hydrothermal reduction of $K_3[Fe(CN)_6]$ (102.8 Oe) [35] and hydrothermally synthesized $FeO.Fe_2O_3$ octahedra (74 Oe) [35]. The MR of $FeO.Fe_2O_3$-NTPI composite and precursor $FeO.Fe_2O_3$ nanoparticles are 0.08 and 0.1 emu g^{-1}, respectively. The MR of precursor $FeO.Fe_2O_3$ is much smaller than those of hydrothermally synthesized $FeO.Fe_2O_3$ octahedra (4.2 emu g^{-1}) [35] and $FeO.Fe_2O_3$ microoctahedra (13.5 emu g^{-1}), obtained by hydrothermal reduction of $K_3[Fe(CN)_6]$ [35]. The insignificant MR values of precursor $FeO.Fe_2O_3$nanoparticles and $FeO.Fe_2O_3$-NTPI nanocomposite indicate their superparamagnetic behavior. Further, the saturation magnetization (MS) of $FeO.Fe_2O_3$-NTPI nanocomposite (1.0 emu g^{-1}) is not significantly different from that of

$FeO.Fe_2O_3$ nanoparticles (1.5 emu g^{-1}). The synthesized $FeO.Fe_2O_3$-NTPI nanocomposite is easily recoverable from the dispersed medium using a magnet. Figure 10b presents the effective separation of the nanocomposite with a handy magnet. All the particles of the synthesized composite are attracted by the magnet. This shows the absence of formation of bare NTPI during the synthesis of $FeO.Fe_2O_3$-NTPI nanocomposites

3.5. FT-IR spectra of NTPI, pristine $FeO.Fe_2O_3$ *and* $FeO.Fe_2O_3$*–NTPI composite*

The FT-IR spectra of NTPI, $FeO.Fe_2O_3$ nanoparticles and $FeO.Fe_2O_3$–NTPI composite, are shown in Figure 11 and the prominent frequencies are displayed in Table 2. The $FeO.Fe_2O_3$ nanoparticles show strong bands at 3437, 2923, 2855, 1742, 1633, 1457, 1383, 1112, 1022, 697, 640 and 567 cm^{-1}.

The peak at 3437 cm^{-1} is likely due to the adsorption of water molecules as this is the frequency widely associated with –OH stretching.The band at 567 cm^{-1} is related to the Fe–O bending vibration, whereas the band at 574 cm^{-1} in $FeO.Fe_2O_3$–NTPI composite is an indication of the presence of N–Fe–O stretching vibration. The Fe-O stretching vibration of $FeO.Fe_2O_3$nanoparticles is shifted from 567 to 574 cm^{-1} and this may be due to the binding of NTPI with the superparamagnetic nanoparticles. The frequency around 1600 cm^{-1} corresponds to C=N function of NTPI and $FeO.Fe_2O_3$-NTPI composite. The peak around 3426 cm^{-1} corresponds to ≥ N-H in NTPI and $FeO.Fe_2O_3$–NTPI composite and the peak at ~ 745 cm^{-1} is likely due to the aromatic C-H bending.

3.6. Photoconductivity of pristine $FeO.Fe_2O_3$ *and NTPI-*$FeO.Fe_2O_3$ *composite*

Photoconductivities of both pristine $FeO.Fe_2O_3$and NTPI-$FeO.Fe_2O_3$ have been studied and the I–V characteristics of the samples have been shown in Figure 12a & b. The variation of dark current (I_{dc}) and photocurrent (I_{pc}) with applied cell voltage on a log–log scale in the dark and

under UV light illumination is shown for both pristine and composite. These two graphs represent the linear variation with different slopes and can be expressed by the power law, *i.e.* $I \alpha V^r$, where I is either I_{pc} or I_{dc}, V is the applied DC voltage and the exponent 'r' is the slope of straight line segment of the log–log plot. The variation of I_{dc} and I_{pc} with applied voltage displayed by $FeO.Fe_2O_3$ is found to be non-ohmic super linear [36-38] in nature, *i.e.,* the power index is $1 < r < 2$. The non-ohmic superlinear variation ($1 < r < 2$) in the dark current and photocurrent suggests that the charge carriers are being injected into the bulk of the materials produced from one of the electrodes [36] originated from the surface adsorbed oxygen or hydroxyl species.This photoresponse confirms the features of the sample itself, but not the features of the sample-contact region. Though the dark current and photocurrent for both the samples increases with increase of voltage, the dark current and photocurrent of composite is lower than that of bare $FeO.Fe_2O_3$. Adsorption of NTPI on the surface of $FeO.Fe_2O_3$ is likely to be the reason for the decrease of dark current as well as the photocurrent.

Initially the field dependent dark current starts decreasing slowly until it reach a steady value due to the field induced adsorption of oxygen molecules as well as to the presence of defects [39]. In the absence of UV light, the adsorbed oxygen picks up a free electron from the surface of the pristine $FeO.Fe_2O_3$ and the composite particles become negatively charged ions [$O_2 + e^- \text{-----} > O_2^-{}_{(ad)}$] and develops a depletion layer leading to low conductivity [40-42]. Furthermore, the photocurrent of $FeO.Fe_2O_3$-NTPI is reduced significantly when compared to pristine $FeO.Fe_2O_3$ which may be explained on the basis of adsorption/desorption processes on the surface of the samples. The concentration of adsorbed oxygen molecules on the $FeO.Fe_2O_3$ surface depends on the concentration of dangling bonds on the surface of the sample and as the surface to volume ratio in nano $FeO.Fe_2O_3$ is large, the surface phenomena of adsorption/desorption plays a

significant role. Oxygen molecules get adsorbed on the surface of $FeO.Fe_2O_3$ and when the surface is illuminated by UV-vis light, the photogenerated electron-holes are produced photogenerated holes release the adsorbed oxygen in air [$O_2^-{}_{(ad)} + h^+$------> $O_{2(g)}$] from the surface of $FeO.Fe_2O_3$ which lowers the barrier height for the electrons in the $FeO.Fe_2O_3$ [43], When all photoinduced holes react with O_2^-, the photo-current gets saturated in pristine $FeO.Fe_2O_3$. The photoinduced electrons gives rise to the photocurrent in the pristine $FeO.Fe_2O_3$whereas in composite, the surface of $FeO.Fe_2O_3$ nanoparticles is passivated with the adsorption of NTPI that results in the reduction of adsorption sites for O_2 molecules (Figure 12c).

The photocurrent in the composite may be attributed to the desorption of O_2 molecules from the surface of the NTPI layer as well as from the surface of the non-passivated $FeO.Fe_2O_3$ nanoparticles. As the surface to volume ratio gets lowered in the nanocomposite in comparison with pristine $FeO.Fe_2O_3$ nanoparticles reduction in photocurrent is observed. Lower desorption of O_2 molecules in composite also results in lowering of photocurrent. A few electrons which tunnel through the NTPI layer help O_2 to get adsorbed on the $FeO.Fe_2O_3$ surface under dark conditions, whereas upon UV illumination, the photogenerated holes release O_2 molecules, which cannot come out from the interfacial region. As a result, the electrons are accumulated on the composite interface. Anomalous behavior of photocurrent in the composite may be attributed to the re-adsorption of the desorbed O_2 molecules on the surface of the non-passivated $FeO.Fe_2O_3$ nanoparticles. Because of the adsorption and desorption mechanism of oxygen occurring simultaneously under continuous illumination, we observe drop in the photocurrent giving rise to the negative PC. After the UV light is switched off, the decay current follows the oxygen adsorption mechanism [44,45]. Thus, when the illumination is terminated, the current reduces faster due to the fast recombination of the electrons and holes.

3.7. *Optical properties of nanoaggregates of FONs and NTPI-FeO.Fe$_2$O$_3$ composites*

The UV-vis spectrum (Figure 13a) of NTPI in THF shows absorption bands at 264, 231 and 337 nm. Increasing water content in solution leads to an upward shift with the appearance of a level-off long wavelength tail, which is attributed to Mie scattering due to the formation of nanoaggregates [46]. The AIEE phenomena were conveniently demonstrated by emission spectra of NTPI in various ratios of H_2O/THF solvents (Figure 13b). The emission maximum of NTPI varies significantly with H_2O/THF composition. NTPI in pure THF displays weak green fluorescence at 408 nm on excitation at 270 nm. An enhancement of emission intensity is observed by the addition of water (90%) along with a red shift emission at 486 nm. NTPI in water is expected to change the micro environment, inducing nucleation and growth of the molecules to nanoparticles. AIEE with red-shift of NTPI arises from the restriction of intramolecular rotation (RIR). Single bond rotation is responsible for the dominant non-radiative decay and hence the RIR effect might be the reason for AIEE nature of NTPI. The rotation in the aggregates was restricted by blocking the non-radiative path and activating the radiative decay. The solution of FONs of NTPI is visibly transparent and soluble at room temperature for more than two months. Effect of pH (1-10) on the emission shows that fluorescent NTPI FONs is stable [47].

Interesting spectral properties, photostability and the presence of azomethine nitrogen and thiophene moiety with AIEE properties of FONs prompted us to investigate its behaviour toward different nano metal oxides [48]. The electronic spectral properties of FONs NTPI in H_2O–THF (9: 1, v/v) by the addition of different nano metal oxides viz., FeO.Fe2O3, Fe_2O_3, WO_3, Al_2O_3 and CuO was carried out. The UV-vis spectra of FONs NTPI with the addition of nano FeO.Fe2O3 (90 %) resulted in an increase in absorbance over the entire spectral range from 330

to 500 nm with a level-off tail (Figure 13c). This appearance of level-off tail in the visible region suggests that Fe^{3+} interact with nanoaggregates of NTPI to form larger aggregates leading to scattering phenomena [49,50]. The fluorescence spectrum of NTPI in H_2O–THF (9: 1, v/v) exhibits an emission band at 408 nm. Among the various nano metal oxides tested, *Viz.,* FeO.Fe2O3, CuO,WO_3, Al_2O_3, Fe_2O_3, addition of Fe^{3+} ions to the FONs NTPI leads to switch on the emission (Figure 13d).

The absorbance increased by the addition of low concentration (10 %) of nano FeO.Fe_2O_3 to NTPI and maximum is observed at 90 % (Figure 14c). Similarly emission intensity increased by the addition of low concentration (10 %) of nano FeO.Fe_2O_3 to NTPI and maximum enhancement is observed at 90 % (Figure 14d). The fluorescence quantum yield [51] of nanoaggregates of NTPI and NTPI-FeO.Fe_2O_3 composite was found to be 0.56 and 0.45, respectively. The increase in the fluorescence intensity of nanoaggregates of NTPI upon the addition of nano FeO.Fe_2O_3 is attributed to the interaction of Fe^{3+} ions with nanoaggregates of NTPI and form larger aggregates [49]. A Stern–Volmer plot (Figure 14a) shows the linear dependence of the fluorescence intensity ratio (I_0/I) at a lower concentration of nano FeO.Fe_2O_3. The plot bend upward at higher concentration of metal oxide, which indicates that the mechanism involved for the emission of FONs NTPI by FeO.Fe_2O_3 is due to complexation rather than collisional deactivation [52] and involves cooperative binding in which one Fe^{3+} is coordinated with nitrogen and sulphur atoms of FONs NTPI [49]. The calculated Stern–Volmer constant is 5.7×10^7 M^{-1} which indicates the high sensitivity of nanoaggregates of NTPI towards Fe^{3+}. The formation of this complex leads to charge transfer from the LUMO of the imidazole to the CB of nano FeO.Fe_2O_3 (Figure 14b). Figure 14b presents the HOMO and LUMO energy levels of fluorophore and the CB and VB edges of pristine FeO.Fe_2O_3 nanoparticles. The electron in the LUMO of the excited molecule is

of higher energy than that in the CB of the semiconductors. This should lead to transfer of electron from LUMO of the excited molecule to the CB of $FeO.Fe_2O_3$. The excess energy is released in the form of light and the emission wavelength corresponding to the excess energy is 408 nm. This additional path of emission opened, besides the LUMO→HOMO and deep level emission (DLE), accounts for the enhancement of fluorescence. That is, on irradiation both fluorophore and pristine $FeO.Fe_2O_3$ nanoparticles are excited. Duel emission is expected due to LUMO→HOMO and DLE transition [53]. Also possible is electron jump from the excited NTPI to the nanopebles. Generally, the electron transfer from the LUMO of the fluorophore to the CB of semiconductor is to quench the fluorophore. However, in the present cases the HOMO energy of the fluorophore matches with that of the CB of pristine $FeO.Fe_2O_3$ and this accidental coincidence results in enhancement of fluorescence.

The energy band diagrams of all materials in NTPI- $FeO.Fe_2O_3$ - ZnO composite used are shown in Figure 14c. The HOMO and LUMO of NTPI are of 2.82 and 0.22 eV; ZnO VB and CB are 2.89 and -0.31 eV and that of Fe_2O_3 are 2.48 and 0.28 eV, respectively. The FeO VB and CB are 2.27 and 0.17 eV. In NTPI- $FeO.Fe_2O_3$ -ZnO composite, the direction of CT depending on the relative VB and CB energies of the metal oxides as well as the HOMO and LUMO levels of the adsorbed imidazole molecule. From Figure 14b, it can be seen that there is a barrier for hole injection (HIB) barrier from ZnO VB to NTPI HOMO is too small (0.07 eV). There is only small electron injection (EIB) barrier between NTPI LUMO and ZnO. The excited electron in the CB of FeO is capable of moving to the CB of Fe_2O_3 and CB of ZnO energy levels. The electron generated in the CB of ZnO due to photoexcitation and also the electron slipped from the CB of ZnO is energetically at favourable position to move to the LUMO of NTPI. The hole formed at the VB of ZnO can move to the HOMO of the ligand and the hole and the electron of the

HOMO and the LUMO of NTPI may combined and emits light. Hence the probable electron transfer direction is $FeO.Fe_2O_3$-to-NTPI-to-ZnO and probable hole transfer direction is $FeO.Fe_2O_3$to ZnO to NTPI. So the electron and hole recombination at the NTPI-ZnO interface results in the charge transfer resonance through NTPI molecule. The imidazole molecule can interact with $FeO.Fe_2O_3$ and ZnO surface in such a way that there is a large increase in molecular polarizability (α).

To investigate the nature of the bonding between NTPI and Fe^{3+}, the binding stoichiometry of NTPI with Fe^{3+} was determined by using a job plot in a THF solvent system, where NTPI was completely in the non-aggregated form. The Job plot of the fluorescence emission intensity of NTPI with Fe^{3+} showed a maximum at a mole fraction [NTPI]/([NTPI] + [Fe^{3+}]) 0.5, indicating the formation of 1 : 1 complex. To further confirm the binding interactions between NTPI and Fe^{3+}, the mass spectrum of the complex between NTPI and Fe^{3+} was recorded. An ion peak at m/z 657 corresponding to [NTPI + $FeO.Fe_2O_3$] was clearly observed in the mass spectrum (Figure S1). These results support the idea that NTPI forms 1 : 1 complex with Fe^{3+}. No appreciable change in emission behavior of nanoaggregates was observed in the presence of other nano metal oxides such as CuO, WO_3, Al_2O_3 and Fe_2O_3. Competitive experiments were conducted in the presence of 90 % of nano $FeO.Fe_2O_3$ mixed with 90 % of other nano metal oxides. No significant change in the fluorescence intensity was observed by comparison with or without other metal ions (Figure 15) and the calculated detection limit was found to be 98 x 10^{-9} M for Fe^{3+} ions. The SEM image of FONs in the solvent mixture of H_2O–THF (9 : 1) shows the presence of nanoaggregates (Figure 4) whereas the SEM image of FONs of NTPI-$FeO.Fe_2O_3$ shows bigger aggregates having irregular shape. Further, the SEM-EDX spectrum of nanoaggregates of NTPI-$FeO.Fe_2O_3$ shows the existence of iron, nitrogen and sulphur (Figure 5) which reveal that the interaction of Fe^{3+} with nanoaggregates of NTPI and support the enhancement mechanism (Scheme 1). Emission analysis of nanoaggregates of NTPI with the

ethylenediamine tetracetic acid-ferric complex [iron(III)–EDTA] reveal that the emission intensity of nanoaggregates increases with the addition of the iron(III)– EDTA complex. This shows that nanoaggregates of NTPI can also detect Fe^{3+} ion in the chelate state.

Dipcoating a solution of NTPI on whatman filter paper was dried under vacuum. About 3 μL nano $FeO.Fe_2O_3$ of different concentrations were placed on NTPI coated test strips (Figure S2). The minimum amount of nano $FeO.Fe_2O_3$, detectable by the naked eye, was calculated to be 10.98 pg which shows that the nanoaggregates of NTPI can be used as an efficient, sensitive and selective sensor for Fe^{3+} with a picogram detection limit. Biological applicability of NTPI to nano $FeO.Fe_2O_3$ was analysed by fluorescence spectrum of imidazole in H_2O–THF (9 : 1) with Fe^{3+} ion in the presence of different concentrations of blood serum [54], enhancing the fluorescence emission of nanoaggregates was observed with the addition of nano $FeO.Fe_2O_3$ (Figure S2). This shows that nanoaggregates of NTPI is an efficient fluorescent sensor for the detection of Fe^{3+} ion even in the presence of blood serum.

3.8. Lifetime analysis

The fluorescence decay of pristine $FeO.Fe_2O_3$, NTPI and $FeO.Fe_2O_3$-NTPI composite follow biexponential kinetics (Figure 16). The observed emission lifetime (τ) is indicative of the fact that the phenanthrimidazole interacts with nano $FeO.Fe_2O_3$. The determined radiative (k_r) and nonradiative (k_{nr}) rate constants are displayed in Table 3. The radiative emission of $FeO.Fe_2O_3$-NTPI composite is larger than those of NTPI. The life time studies reveal that the electron is transferred from the excited NTPI to $FeO.Fe_2O_3$ nanoparticles. The rate constant for electron transfer (k_{et}) can be calculated by using the equation, $k_{et} = 1/\tau_{ads} - 1/\tau$ and the calculated k_{et} is

given in Table 3. The electron transfer efficiency is obtained using the equation, E% = (1-$\tau_{composite}/\tau_{NTPI}$) x 100. The unique binding interaction of nanocrystals with organic molecules can be explained on the basis of the larger surface curvature of the nanocrystals which reduces the steric hindrance between the surface binding molecules and provides a larger number of unsaturated dangling bonds on the nanocrystal surface. Hence it is relevant to probe the binding interaction of nano clusters with NTPI.

3.9. Electronic properties of iron oxide clusters and FeO-NTPI composites

In order to get a better insight on the nature of binding of the imidazole with the Fe_2O_3 surface, DFT calculations have been made with iron oxide clusters of different geometries. Fe_3O, Fe_3O_2, Fe_3O_3 and Fe_3O_4, are the clusters used for the calculation. The optimized geometries of iron oxide clusters and its FeO-NTPI composites are shown in Figure 17 and the optimization parameters, energy gap (E_g) and binding energies (E_b) are given in Table 4. The binding interaction between imidazole with the clusters can be analysed by binding energy, $E_b = E_{complex}-(E_{clusters} + E_{NTPI})$, where $E_{complex}$ is the total energy of NTPI adsorbed on the clusters and $E_{clusters}$ and E_{NTPI} are the energies of the iron oxide clusters and NTPI, respectively. From the optimized parameters and binding energies it is confirmed that the iron atom of clusters prefer to bind with azomethine nitrogen and sulphur atoms of NTPI. There is an overlap occurring between the d-orbital of iron and azomethine nitrogen and sulphur atoms which lead to a greater binding energy [55]. The calculated binding energy (E_b) is of the order: Fe_3O_4–NTPI (6.89 eV) > Fe_3O_3–NTPI (6.02 eV) > Fe_3O_2–NTPI (5.81 eV) > Fe_3O–NTPI (5.53 eV). This order is further supported by Fe–N bond distance. The Fe–N bond distance of Fe_3O_4–NTPI composite is shorter (2.02 A^0) than those of Fe_3O_3–NTPI (2.04 A^0), Fe_3O_2–NTPI (2.08A^0) and Fe_3O–NTPI (2.09 A^0). The preferred Fe_3O_4–NTPI composite is stable as compared to other composites [56].

In the optimized bare iron oxide clusters, the Fe–O bond length varies from 1.89 Å to 2.01 Å. Due to the adsorption of NTPI on iron oxide clusters, the surface structure of the $Fe_3O_4$is slightly distorted. Thus the bond length of the composite is expanded by a smaller amount (2.03 Å-2.09 Å). The Fe–O bond is mainly ionic in nature and charge transfer occurs from iron atom to more electronegative oxygen atom and charge transfer is large in the surface region. To analyse the extent of fractional charge transfer from NTPI to iron oxide clusters, we have shown the Mulliken charge of the atoms of bare iron oxide clusters, NTPI and NTPI–iron oxide composites (Table S1). From the Mulliken charge analysis it is clear that there are relatively large changes in the fractional charge of the atoms which bind to the iron oxide nanomaterials and also the atoms adjacent to them. For iron oxide clusters, the oxygen atom exhibits negative charge, which are donor atoms and iron atom exhibits a positive charge, which is an acceptor atom for iron oxide clusters. All hydrogen atoms have positive charges. The iron atom exhibits a more positive charge and the azomethine nitrogen atom exhibits a more negative charge; these atoms favor the weak interaction in imidazole –iron oxide composites.

Energy gap (E_g) of NTPI, Fe_3O–NTPI, Fe_3O_2–NTPI, Fe_3O_3–NTPI and Fe_3O_4–NTPI are 3.8, 1.83, 1.90, 1.98 and 2.01, respectively (Figure 18). A large HOMO–LUMO energy gap implies higher stability and lower chemical reactivity and vice versa [57]. This shows that binding of imidazole on iron oxide cluster induces some changes in the electronic properties and the E_g values are decreased when compared with both bare NTPI and iron oxide clusters. The HOMO–LUMO analysis explains the charge transfer taking place within the NTPI–iron oxide composites. Figure 19 shows the HOMO–LUMO electron distribution plots for NTPI and the composites. The lower energy gap shows that the charge transfer in the Fe_3O_4–NTPI composite is faster than the same in other composites.

3.10. Evidence for linkage

Although there are three basic sites in NTPI, the azomethine nitrogen and sulphur atoms are involved in the binding process with Fe_3O_4 nanoparticles because of the high electron densities. This is supported by molecular electrostatic potential (MEP) for the bare and composites. The MEP map (Figure 20) shows that nitrogen and sulphur atoms represent the most negative potential region (dark red) and green region corresponds to a potential halfway between the two extremes red and dark blue colour.

4. Conclusions

In summary, we could successfully synthesize nano $FeO.Fe_2O_3$, NTPI, FONs of NTPI and $FeO.Fe_2O_3$-NTPI nanocomposite. We observed enhanced PL and negative PC for the NTPI-$FeO.Fe_2O_3$ nanocomposite material. Pristine nano $FeO.Fe_2O_3$ exhibits a decreased PL emission but show enhanced PC. The enhanced PL emission in the $FeO.Fe_2O_3$ -NTPI composite is attributed to the reduction of the non-radiative trap levels at the interfaces of the $FeO.Fe_2O_3$-NTPI. $FeO.Fe_2O_3$ composite formation with NTPI reduces the oxygen adsorption sites and the tunneling of electrons among the particles leads to negative photoconductivity in $FeO.Fe_2O_3$-NTPI nanocomposite. To conclude, pristine $FeO.Fe_2O_3$can be used for UV photodetection and optical switches and, the $FeO.Fe_2O_3$-NTPI nano-composite can find application in development of luminescent materials due to their enhanced PL intensity. The NTPI with nitrogen and sulphur atoms forms fluorescent organic nanoparticles which can work as an efficient and selective fluorescent sensor for the detection of Fe^{3+} ions at the pictogram level. The radiative emission of $FeO.Fe_2O_3$-NTPI composite is larger than those of NTPI. The life time studies reveal that the electron is transferred from the excited NTPI to $FeO.Fe_2O_3$ nanoparticles. The calculated binding

energies (E_b) are of the order: Fe_3O_4–NTPI (6.89 eV) > Fe_3O_3–NTPI (6.02 eV) > Fe_3O_2–NTPI (5.81 eV) > Fe_3O–NTPI (5.53 eV).

5. Acknowledgments

One of the authors Prof. J. Jayabharathi is thankful to CSIR [No. 01/(2707)/13EMR-II], DST [No. SR/S1/IC-73/2010], DRDO (NRB-213/MAT/10-11) and UGC (F.No. 36-21/2008) for providing funds to this research study. Mr. A. Prabhakaran is thankful to for CSIR [No. 01/(2707)/13EMR-II], providing fellowship.

References

[1] R. Chen, G. Song and Y. Wei, *J. Phys. Chem. C.,* 2010, **114**, 13409.

[2] G. Schmid and D. Fenske, *Phil. Trans. R. Soc. A.,* 2010, **368**, 1207.

[3] M. L-r, W. Chen, Y. Tan, L. Zou, C. Chen, H. Zhou and Q. Peng, Y. Li, *Nano Res.,* 2011, **4 (4)**, 370.

[4] J.K. Oh and J.M. Park, *Prog. Polym. Sci.,* 2011, **36**, 168.

[5] D. Pan, H. Zhang, T. Fan, J. Chen and X. Duan, *Chem. Commun*., 2011, **47**, 908.

[6] J. Alam, U. Riaz, S.M. Ashraf, S. Ahmad and J. Coat. *Technol. Res*., 2008, **5**, 123.

[7] M. Mahmoudi, H. Hosseinkhani, M. Hosseinkhani, S. Boutry, A. Simchi, W.S. Journeay, K. Subramani and S. Laurent, *Chem. Rev*., 2011,**111**, 253.

[8] S. Liang, M. Li, J. H. Wang, X. L. Liu, Z. H. Hao, L. Zhou, X. F. Yu and Q. Q. Wang, *Opt. Express.,* 2013, **21**, 3253–3258.

[9] S. Panigrahi and D. Basak, *Chem. Phys. Lett.,* 2011, **511**, 91– 96.

[10] C. Jin, H. Kim, S. Park, Y. Kwon, S. Lee, H. W. Kim and C. Lee, *Adv. Appl. Ceram.,* 2011, **110**, 270–274.

[11] S. Panigrahi, A. Bera and D. Basak, *ACS Appl. Mater. Interfaces.*, 2009, **1**, 2408–2411.

[12] J. D. Prades, F. H. Ramirez, R. J. Diaz, M. Manzanares, T. Andreu, A. Cirera, A. R. Rodriguez and J. R. Morante, *Nanotechnology.,* 2008, **19**, 465501–465507.

[13] Q. H. Li, T. Gao, Y. G. Wang and T. H. Wang, *Appl. Phys. Lett.,* 2006, **86,** 123117–123119.

[14] Y. Lin, D. Wang, Q. Zhao, Z. Li, Y. Ma and M. Yang, *Nanotechnology.,* 2006, **17**, 2110–2115.

[15] (a) M. Kumar and S. J. George, *Nanoscale.,* 2011, **3**, 2130–2133; (b) S. Yagai, Y. Goto, X. Lin, T. Karatsu, A. Kitamura, D. Kuzuhara, H. Yamada, Y. Kikkawa, A. Saeki and S. Seki,

Angew. Chem., Int. Ed., 2012, **51**, 6643–6647; (c) M. Shellaiah, Y. H. Wu, A. Singh, M. V. R. Raju and H. C. Lin, *J. Mater. Chem. A.,* 2013, **1**, 1310–1318; (d) S. Y. Ryu, S. Kim, J. Seo, Y.W. Kim, O. H. Kwon, D. J. Jang and S. Y. Park, *Chem. Commun.,* 2004, 70–71; (e) B. K. An, S. K. Kwon, S. D. Jung and S. Y. Park, *J. Am. Chem. Soc.,* 2002, **124**, 14410–14415.

[16] (a) H. H. Lin, Y. C. Chan, J. W. Chen and C. C. Chang, *J. Mater. Chem.,* 2011, **21**, 3170–3177; (b) X. Y. Zhang, S. Q. Wang, L. X. Xu, L. Feng, Y. Ji, L. Tao, S. X. Li and Y. Wei, *Nanoscale.,* 2012, **4**, 5581–5584; (c) M. C. Hsieh, C. H. Chien, C. C. Chang and T. C. Chang, *J. Mater. Chem.B.,* 2013, **1**, 2350–2357; (d) H. H. Lin, Y. C. Chan, J. W. Chen and C. C. Chang*, J. Mater. Chem.,* 2011, **21**, 3170–3177.

[17] M. De, P. S. Ghosh and V. M. Rotello, *Adv. Mater.,* 2008, **20**, 4225–4241.

[18] H. Tong, Y. Hong, Y. Dong, M. Haussler, Z. Li, J. W. Y. Lam, Y. Dong, H. H. Y. Sung, I. D. Williams and B. Z. Tang, *J. Phys. Chem. B.,* 2007, **111**, 11817–11823.

[19] M. Wang, D. Zhang, G. Zhang, Y. Tang, S. Wang and D. Zhu, *Anal. Chem.,* 2008, **80**, 6443–6448.

[20] Y. Liu, Y. Tang, N. N. Barashkov, I. S. Irgibaeva, J. W. Y. Lam, R. Hu, D. Birimzhanova, Y. Yu and B. Z. Tang, *J. Am. Chem. Soc.,* 2010, **132**, 13951–13953.

[21] Y. Liu, C. Deng, L. Tang, A. Qin, R. Hu, J. Z. Sun and B. Z. Tang, J. Am. *Chem. Soc.,* 2011, **133**, 660–663.

[22] W. L. Gong, M. P. Aldred, G. F. Zhang, C. Li and M. Q. Zhu, *J. Mater. Chem. C.,* 2013, **1**, 7519–7525.

[23] (a) A. Singh, S. Kaur, N. Singh and N. Kaur, *Org. Biomol. Chem.,* 2014, **12**, 2302 – 2309; (b) G. B. Zhang, A.X. Ding, Y. Zhang, L.M. Yang, L. Kong, X. J. Zhang, X.T. Tao, Y.P.

Tian and J. X. Yang, *Sens. Actuators. B.,* 2014, **202**, 209 – 216; (c) V. K. Bhardwaj, H. Sharma, N. Kaurb and N. Singh, *New J. Chem.,* 2013, **37**, 4192 – 4198.

[24] H. T. Feng, S. Song, Y. C. Chen, C. H. Shen and Y. S. Zheng, *J. Mater. Chem. C.,* 2014, **2**, 2353 – 2359.

[25] H. J. Yan, H. Y. Su, D. M. Tian, F. J. Miao and H. B. Li, *Sens. Actuators, B.,* 2011, **160**, 656 – 661.

[26] M. J. Frisch, G. W. Trucks, H. B. Schlegel, G. E. Scuseria, M. A. Robb, J. R. Cheeseman, J. A. Montgomery, Jr., T. Vreven, K. N. Kudin, J. C. Burant, J. M. Millam, S. S. Iyengar, J. Tomasi, V. Barone, B. Mennucci, M. Cossi, G. Scalmani, N. Rega, G. A. Petersson, H. Nakatsuji, M. Hada, M. Ehara, K. Toyota, R. Fukuda, J. Hasegawa, M. Ishida, T. Nakajima, Y. Honda, O. Kitao, H. Nakai, M. Klene, X. Li, J. E. Knox, H. P. Hratchian, J. B. Cross, C. Adamo, J. Jaramillo, R. Gomperts, R. E. Stratmann, O. Yazyev, A. J. Austin, R. Cammi, C. Pomelli, J. W. Ochterski, P. Y. Ayala, K. Morokuma, G. A. Voth, P. Salvador, J. J. Dannenberg, V. G. Zakrzewski, S. Dapprich, A. D. Daniels, M. C. Strain, O. Farkas, D. K. Malick, A. D. Rabuck, K. Raghavachari, J. B. Foresman, J. V. Ortiz, Q. Cui, A. G. Baboul, S. Clifford, J. Cioslowski, B. B. Stefanov, G. Liu, A. Liashenko, P. Piskorz, I. Komaromi, R. L. Martin, D. J. Fox, T. Keith, M. A. Al-Laham, C. Y. Peng, A. Nanayakkara, M. Challacombe, P. M. W. Gill, B. Johnson, W. Chen, M. W. Wong, C. Gonzalez and J. A. Pople, *Gaussian, Inc., Pittsburgh PA*. 2003.

[27] J. Jayabharathi, V. Thanikachalam and R. Sathishkumar, *J. Fluoresc.,* 2014, **24**, 431.

[28] Y. H. Jin, S. D. Seo, H. W. Shim, K. S. Park and D. W. Kim, *Nanotechnology.*, 2012, **23**, 125402–125407.

[29] B. Sahoo, K. S. P. Devi, S. K. Sahu, S. Nayak, T. K. Maiti, D. Dhara and P. Pramanik, *Biomater. Sci.,* 2013, **1**, 647–657.

[30] Y. Su, G. Li, X. Bo and L. Li, *Nanotechnology.*, 2007, **18**, 485602.

[31] K. Vanheusden, W. L. Warren, C. H. Seager, D. R. Tallant, J. A. Voigt and B. E. Gnade, *J. Appl. Phys.,* 1996, **79**, 7983–7990.

[32] K. Vanheusden, C. H. Seager, W. L. Warren, D. R. Tallant and J. A. Voigt, *Appl. Phys. Lett.,* 1996, **68**, 403–405.

[33] Y. Gong, T. Andelman, G. F. Neumark, S. O'Brien and I. L. Kuskovsky, *Nanoscale Res. Lett.,* 2007, **2**, 297–302.

[34] C. Karunakaran, P. Vinayagamoorthy and J. Jayabharathi, *Langmuir.,* 2014, **30,** 15031−15039.

[35] (a) Wang, W.-W.; and Yao, J.-L.. *Mater.Res. Bull.,* 2010, **45**, 710−716; (b) Zhang, J.; Kong, Q.; Du, J.; Ma, D.; Xi, G.; and Qian, Y. J. *Cryst. Growth.,* 2007, **308**, 159−165; (c) Hu, C.; Gao, Z.; and Yang, X. *Chem. Phys. Lett.,* 2006, **429**, 513−517.

[36] S. K. Mishra, R. K. Srivastava and S. G. Prakash, *J. Alloys Compd.,* 2012, **539**, 1–6.

[37] Z.-M. Liao, Z.-K. Lv, Y.-B. Zhou, J. Xu, J.-M. Zhang and D.-P. Yu, *Nanotechnology.*, 2008, **19**, 335204.

[38] P. K. C. Pillai, N. Shroff, N. N. Kumar and A. K. Tripathi, Phys. Rev. B: *Condens. Matter Mater. Phys.,* 1985, **32**, 8228–8233.

[39] S.K. Mishra, R.K. Srivastava, S.G. Prakash, R.S. Yadav and A.C. Pandey, *Electron. Mater. Lett.,* 2011, **7**, 31 – 38.

[40] Q. H. Li, T. Gao and T.H. Wang, *Appl. Phys. Lett.,* 2005, **86**, 193109 – 193111.

[41] T. Gao, Q. H. Li and T.H. Wang, *Appl. Phys. Lett.,* 2005, **86**, 173105 – 173107.

[42] H. Kind, H. Yan, B. Messer, M. Law and P. Yang, *Adv. Mater.,* 2002, **14**, 158 – 160.

[43] Y. Muraoka, N. Takubo and Z. Hiroi, *J. Appl. Phys.,* 2009, **105**, 103702 – 103708.

[44] Q. H. Li, T. Gao, Y. G. Wang and T. H. Wang, *Appl. Phys. Lett.,* 2005, **86**, 123117 – 123119.

[45] X. G. Zheng, Q. Sh. Li, W. Hu, D. Chen, N. Zhang, M. J. Shi, J. J. Wang and L. Ch. Zhang, *J. Lumin.,* 2007, **122**, 198 – 201.

[46] B. Z. Tang, Y. Geng, J. W. Y. Lam, B. Li, X. Jing, X. Wang, F. Wang, A. B. Pakhomov and X. Zhang, *Chem. Mater.,* 1999, **11**, 1581.

[47] (a) V. Bhalla, A. Gupta and M. Kumar, *Org. Lett.,* 2012, **14**, 3112; (b) C. R. Swartz, S. R. Parkin, J. E. Bullock, J. E. Anthony, A. C. Mayer and G. G. Malliaras, *Org. Lett.,* 2005, **7**, 3163.

[48] (a) L. Duan, Y. Xu and X. Qian, *Chem. Commun.,* 2008, 6339; (b) V. Tharmaraj, S. Devi and K. Pitchumani, *Analyst.,* 2012, **137**, 5320; (c) S. Fu, Z. Liu, S. Liu, J. Liu and A. Yi, *Anal. Chim. Acta.*, 2007, **599**, 271; (d) V. Madhu and S. K. Das, Eur. *J. Inorg. Chem.,* 2006, 1505.

[49] (a) B. Liu, Y. Bao, H. Wang, F. Du, J. Tian, Q. Li, T. Wang and R. Bai, *J. Mater. Chem.,* 2012, **22**, 3555; (b) T. Han, X. Feng, B. Tong, J. Shi, L. Chen, J. Zhi and Y. Dong, *Chem. Commun.,* 2012, **48**, 416; (c) Y. Hong, S. Chen, C. W. T. Leung, J. W. Y. Lam, J. Liu, N.-W. Tseng, R. T. K. Kwok, Y. Yu, Z. Wang and B. Z. Tang, *ACS Appl. Mater. Interfaces.*, 2011, **3**, 3411.

[50] C. F. Bohren and D. R. Huffman, *Absorption and Scattering of Light by Small Particles, Wiley.,* 1983.

[51] J. N. Demas and G. A. Grosby, *J. Phys. Chem.,* 1971, **75**, 991.

[52] Y. Zhang, C. B. Murphy and W. E. Jones, *Macromolecules.,* 2002, **35**, 630.

[53] (a) L. Jing, Y. Qu, B. Wang, S. Li, B. Jiang, L. Yang, W. Fu, H. Fu and J. Sun, *Sol. Energ. Mat. Sol. C.,* 2006, **90**, 1773; (b) L. Zhang, L. Yin, C. Wang, N. Lun, Y. Qi and D. Xiang, *J. Phys. Chem. C.,* 2010, **114**, 9651.

[54] V. Bhalla, A. Gupta and M. Kumar*., Dalton Trans*., 2013, **42**, 4464.

[55] S. Saha and P. Sarkar, *Phys. Chem. Chem. Phys.,* 2014, **16**, 15355 – 15366.

[56] A. V. Kachynski, A. N. Kuzmin, M. Nyk, I. Roy and P. N. Prasad, *J. Phys. Chem. C.,* 2008, **112**, 10721 – 10724.

[57] B. Wang, S. Nagase, J. Zhao and G. Wang, *J. Phys. Chem. C.,* 2007, **111**, 4956 – 4963.

Figure Captions

Figure 1. X-ray diffraction patterns (XRD) of pristine $FeO.Fe_2O_3$ and $FeO.Fe_2O_3$ – NTPI nanocomposites.

Figure 2. HR-TEM images and SAED pattern of pristine $FeO.Fe_2O_3$.

Figure 3. HR-TEM images and SAED pattern of $FeO.Fe_2O_3$ – NTPI nanocomposite.

Figure 4. HR-SEM images of pristine $FeO.Fe_2O_3$ and $FeO.Fe_2O_3$ – NTPI nanocomposite.

Figure 5. EDS of pristine $FeO.Fe_2O_3$ and $FeO.Fe_2O_3$ – NTPI nanocomposite.

Figure 6. DLS and (a and b) and zeta potential (c and d) of pristine $FeO.Fe_2O_3$ and $FeO.Fe_2O_3$ - NTPI nanocomposite.

Figure 7. XPS of pristine $FeO.Fe_2O_3$ and $FeO.Fe_2O_3$ – NTPI nanocomposite.

Figure 8. Diffused reflectance spectra (DRS) of pristine $FeO.Fe_2O_3$, NTPI and $FeO.Fe_2O_3$ – NTPI nanocomposite.

Figure 9. (**a**) Photoluminescence spectra of pristine $FeO.Fe_2O_3$, NTPI and NTPI-$FeO.Fe_2O_3$; (**b**) PL spectra of pristine $FeO.Fe_2O_3$, NTPI and NTPI-$FeO.Fe_2O_3$ composite

Figure 10. (**a**) M-H curves of pristine $FeO.Fe_2O_3$ and $FeO.Fe_2O_3$ -NTPI composite; (**b**) Magnetic recovery image of $FeO.Fe_2O_3$ -NTPI composite

Figure 11. The FT-IR spectra of NTPI, pristine $FeO.Fe_2O_3$ and $FeO.Fe_2O_3$ – NTPI composite

Figure 12. I-V characteristics of (a) pristine $FeO.Fe_2O_3$; (**b**) NTPI-$FeO.Fe_2O_3$ and (**c**) Schematic adsorption and desorption of O_2 molecules.

Figure 13. (**a**) UV-vis spectrum of NTPI in aqueous THF solution; (**b**) Emission spectra of NTPI in aqueous THF solution; (**c**) UV-vis spectra of NTPI with different nanoparticles; (**d**) Emission spectra of NTPI with different nanoparticles.

Figure 14. (**a**) Stern-Volmer plot; (**b**) photoelectron transfer mechanism; (**c**) UV-vis absorption spectra of NTPI with nano $FeO.Fe_2O_3$; (**d**) Emission spectra of NTPI with nano $FeO.Fe_2O_3$.

Figure 15. Competitive experiments of 90 % nano $FeO.Fe_2O_3$ with 90 % other nano metal oxides

Figure 16. Life time spectra of NTPI along with pristine $FeO.Fe_2O_3$ and NTPI –$FeO.Fe_2O_3$ composites

Figure 17. Optimized structures of NTPI, pristine Fe_3O_4 and NTPI – Fe_3O_4 composites

Figure 18. Projected density of states (PDOS) for NTPI, bare $(FeO)_n$ clusters and their imidazole–$(FeO)_n$ composites

Figure 19. HOMO-LUMO contour maps for NTPI, bare $(FeO)_n$ clusters and imidazole–$(FeO)_n$ composites

Figure 20. Molecular electrostatic potential (MEP) diagram of bare $(FeO)_n$ clusters and NSPI – $(FeO)_n$ composites

Scheme 1. Schematic representation of binding of nanoaggregates NTPI with Fe^{3+}

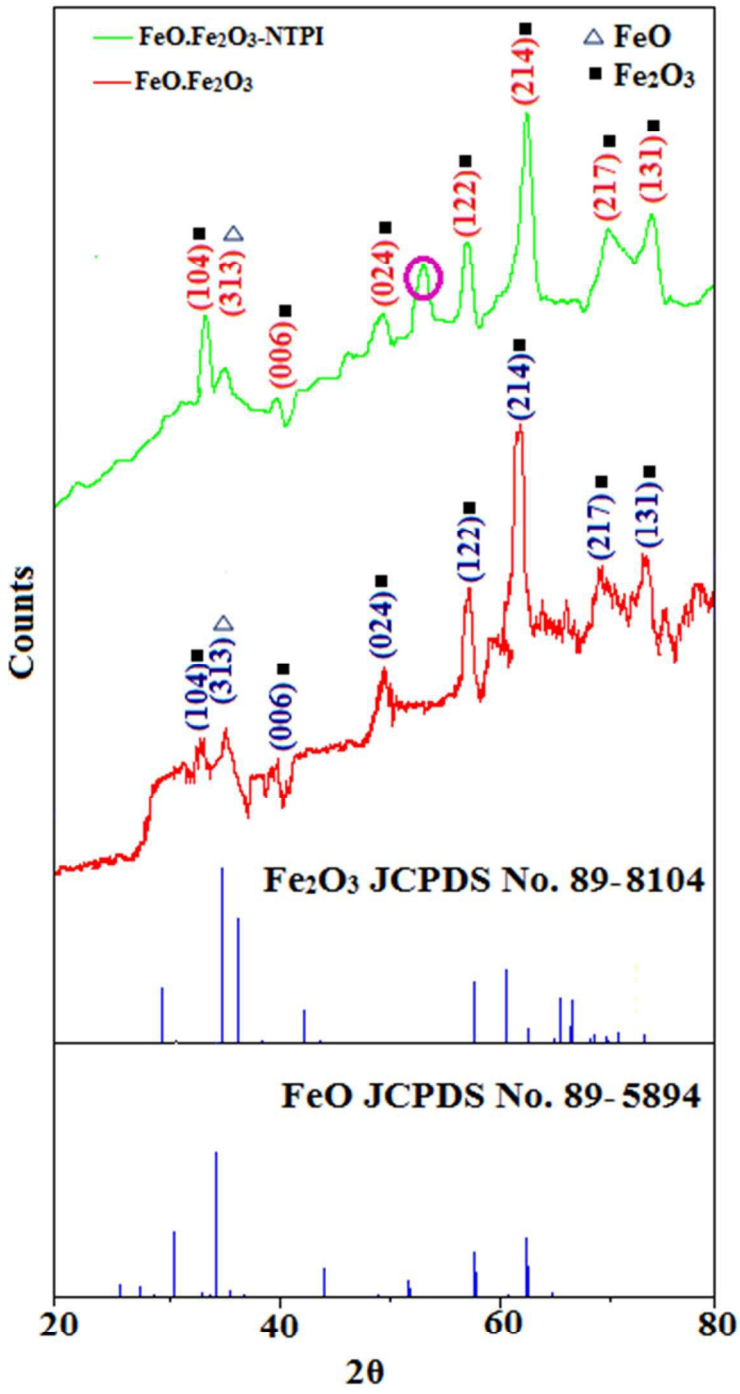

Figure 1

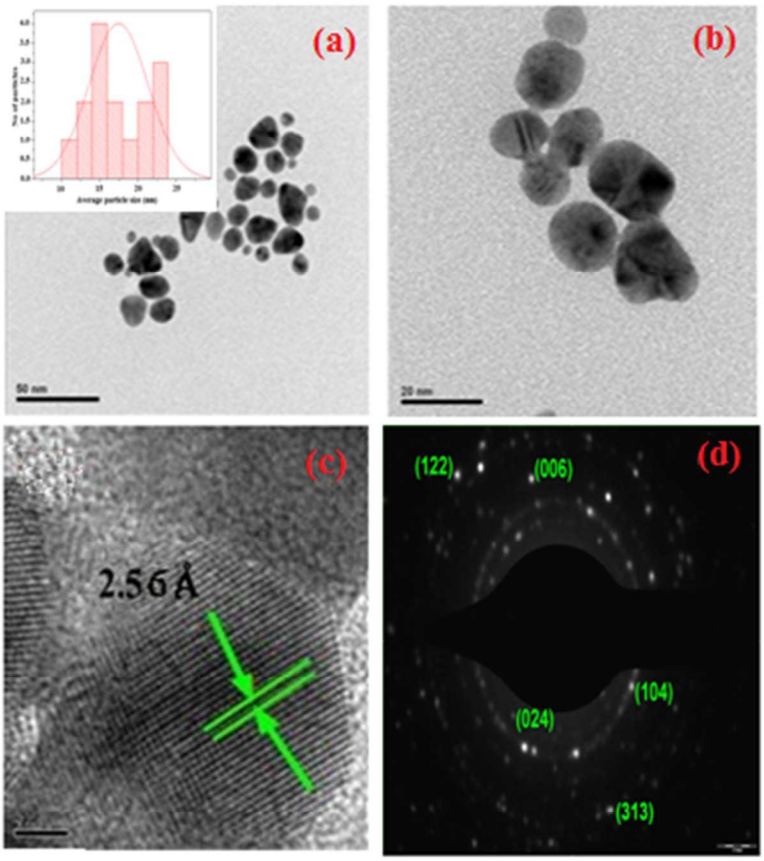

Figure 2

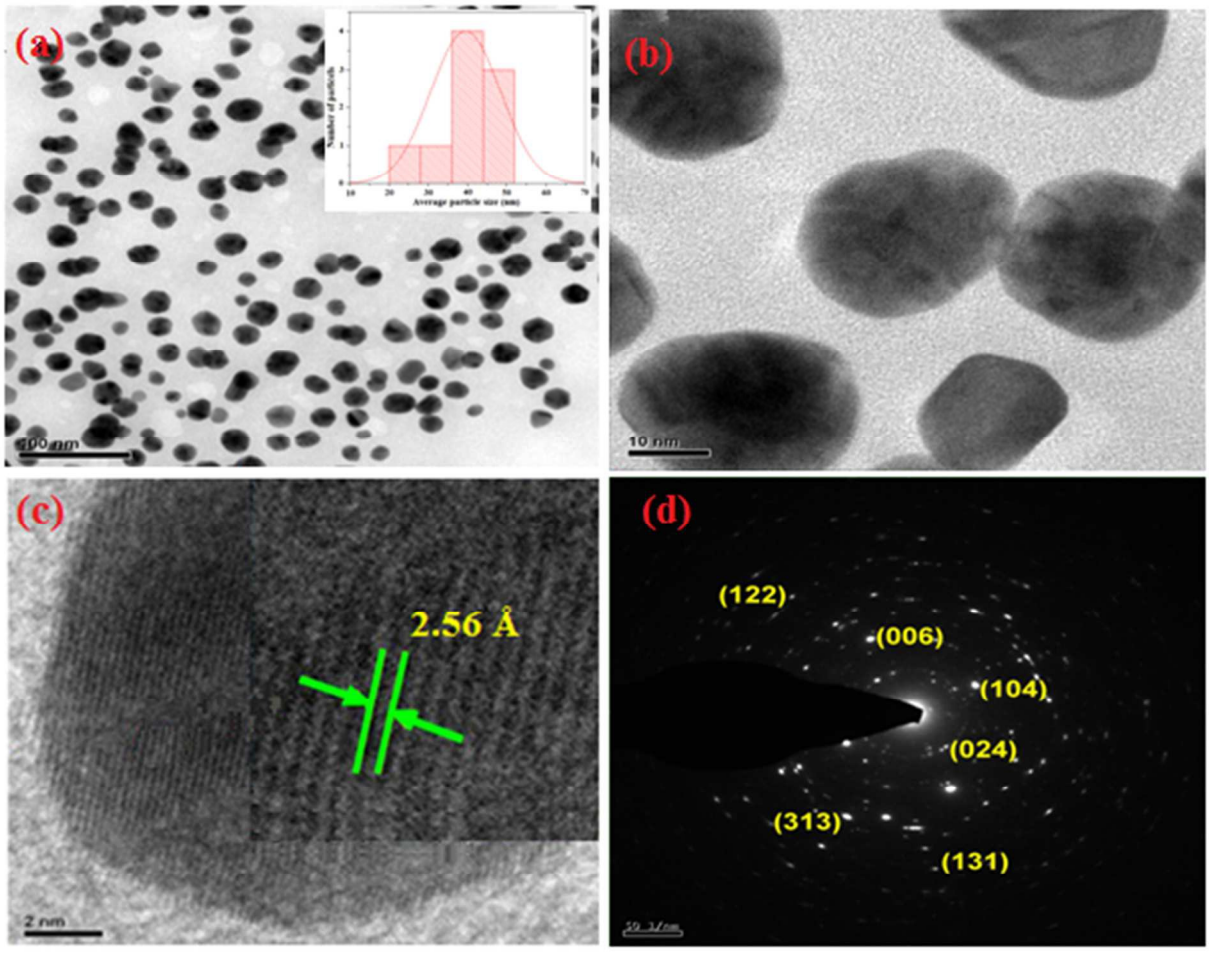

Figure 3

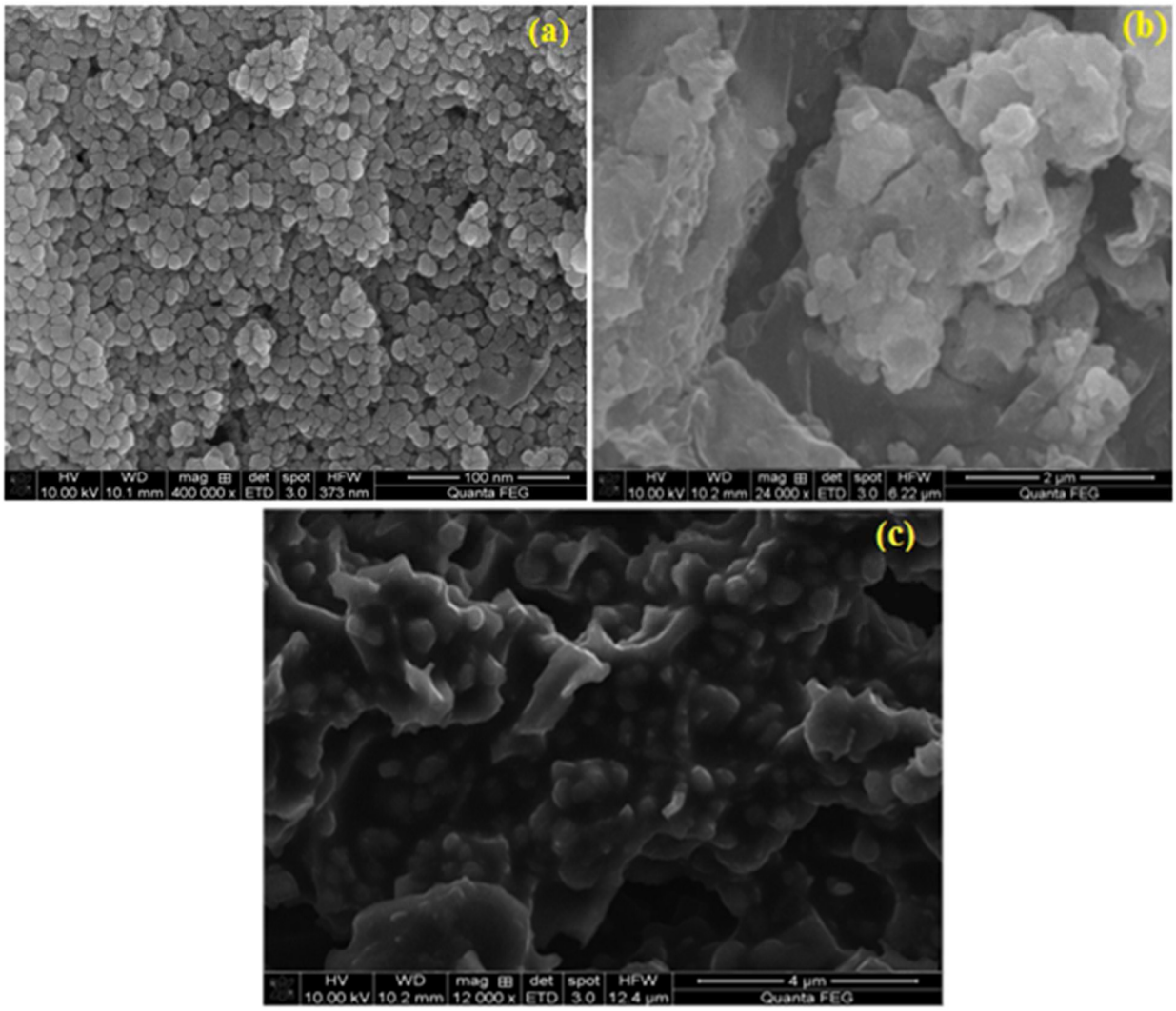

Figure 4

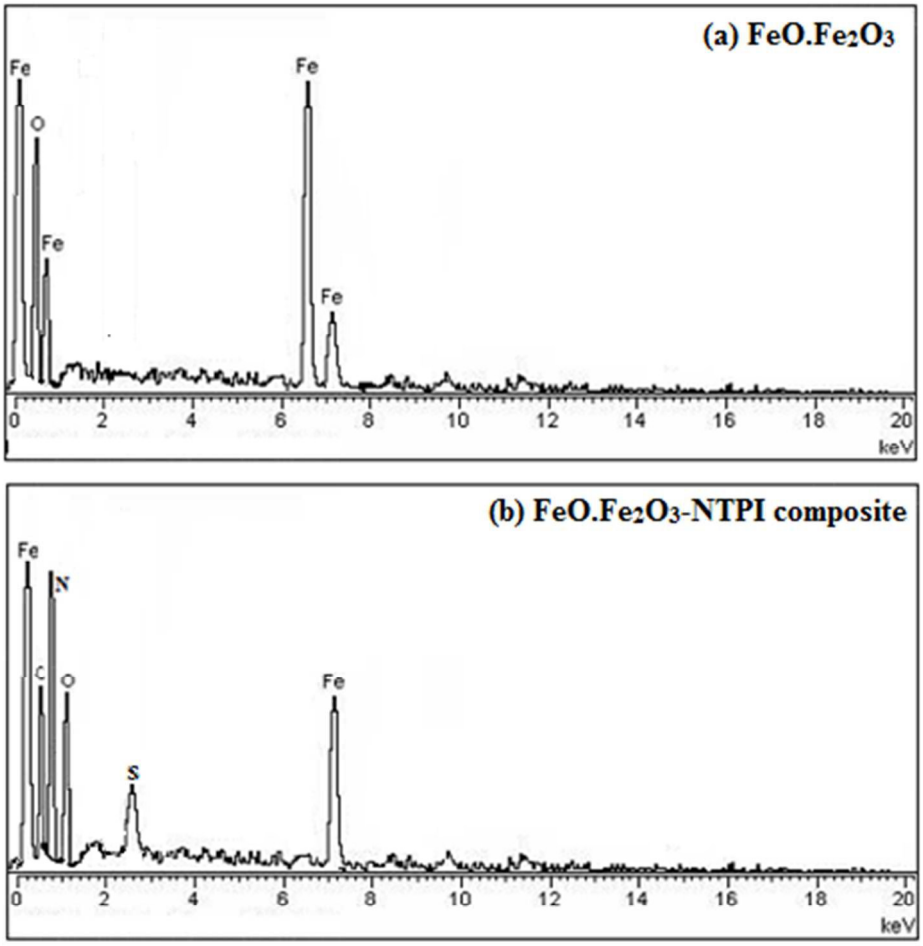

Figure 5

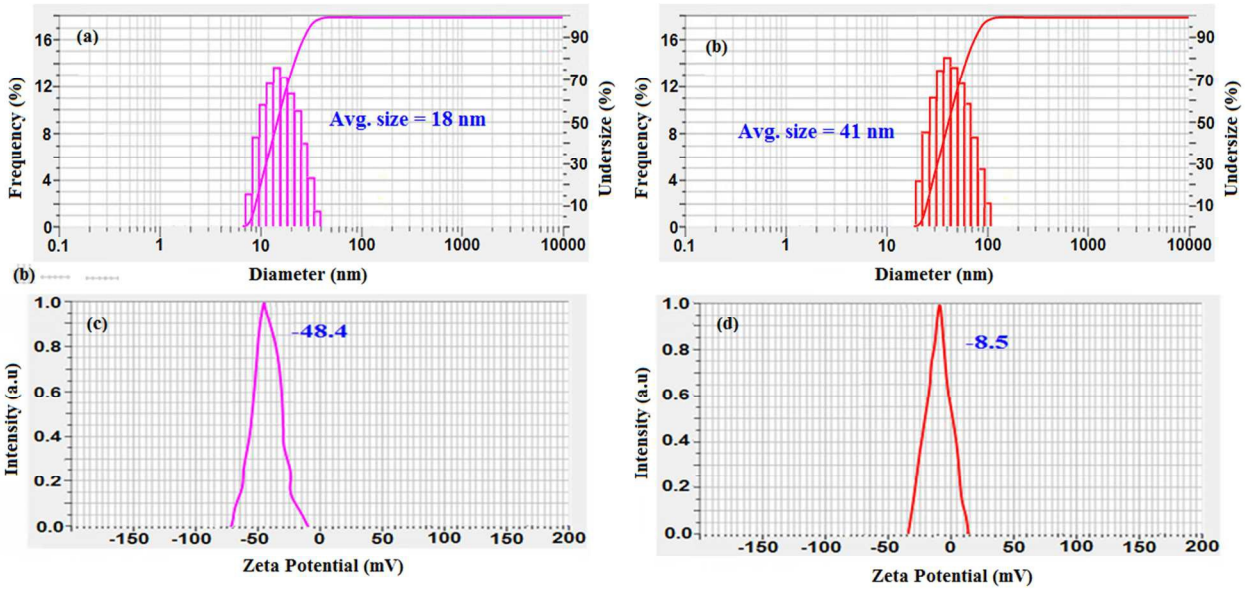

Figure 6

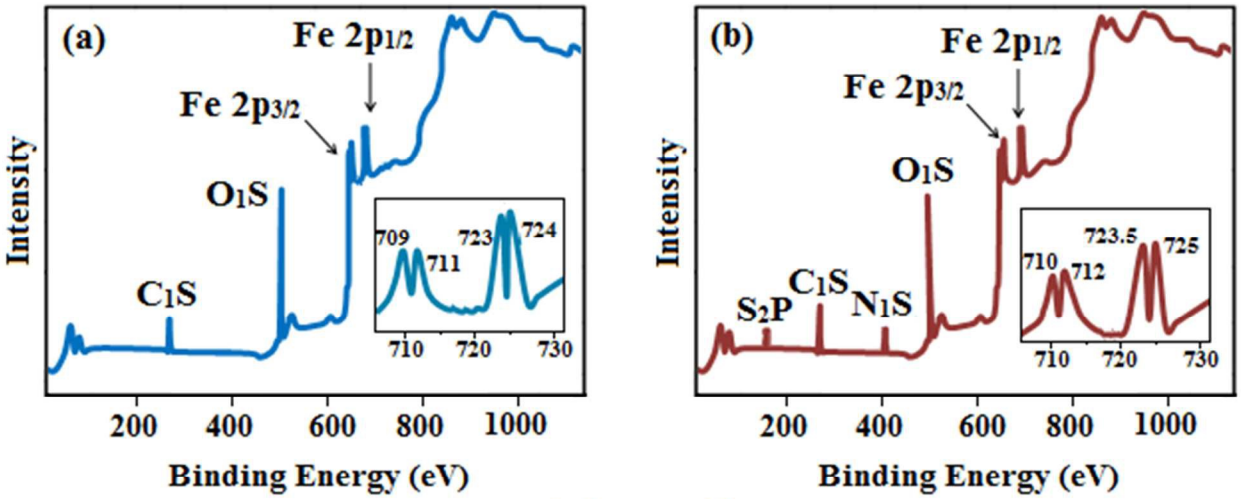

Figure 7

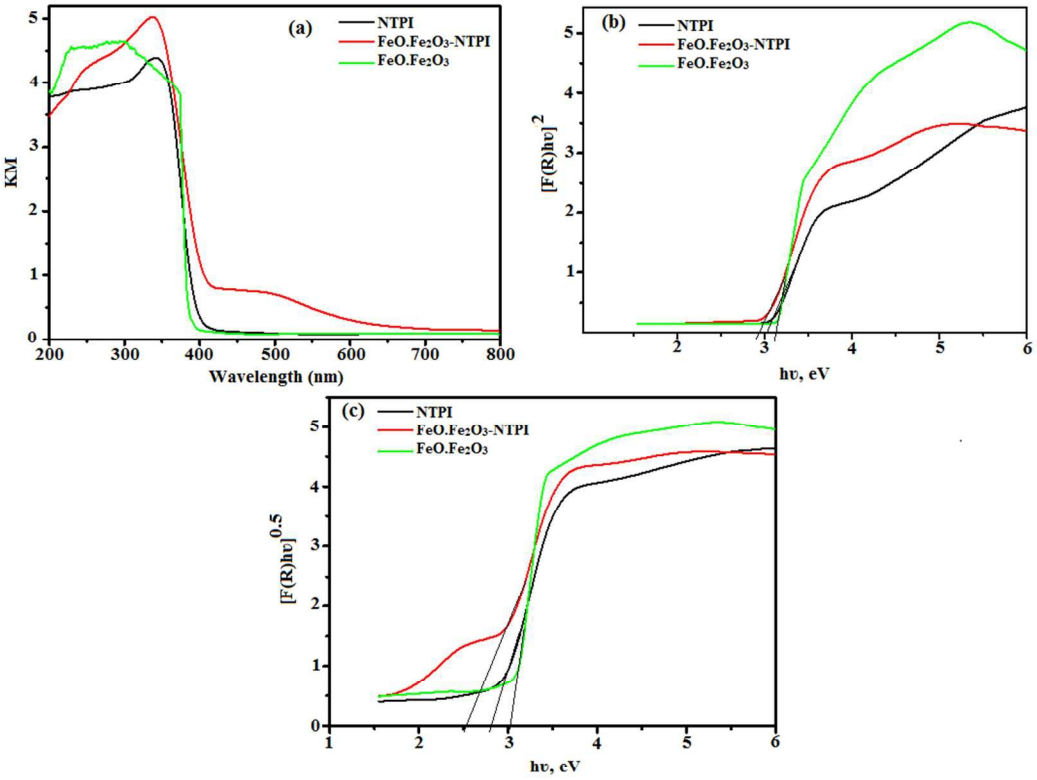

Figure 8

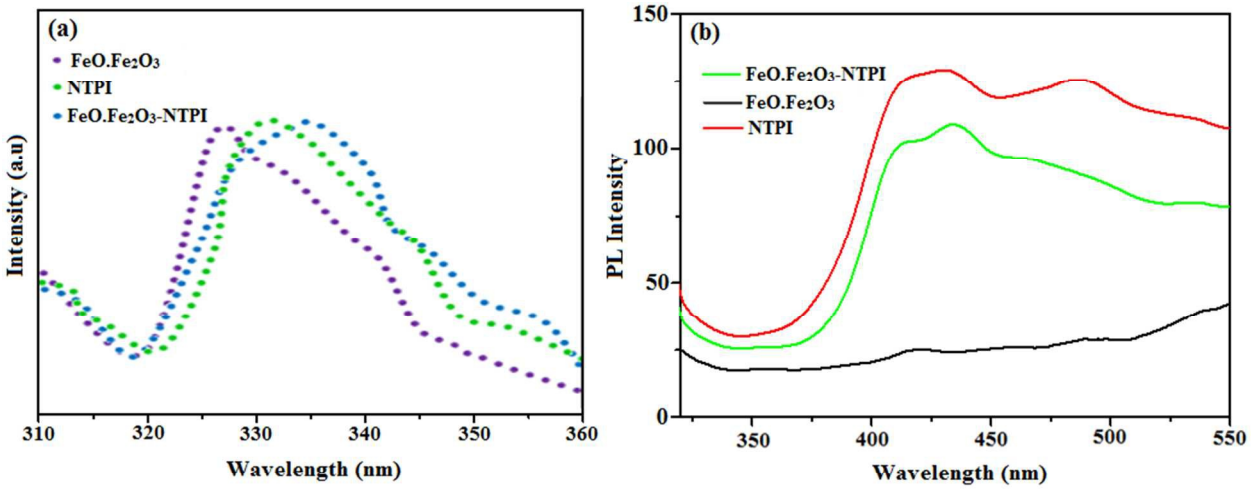

Figure 9

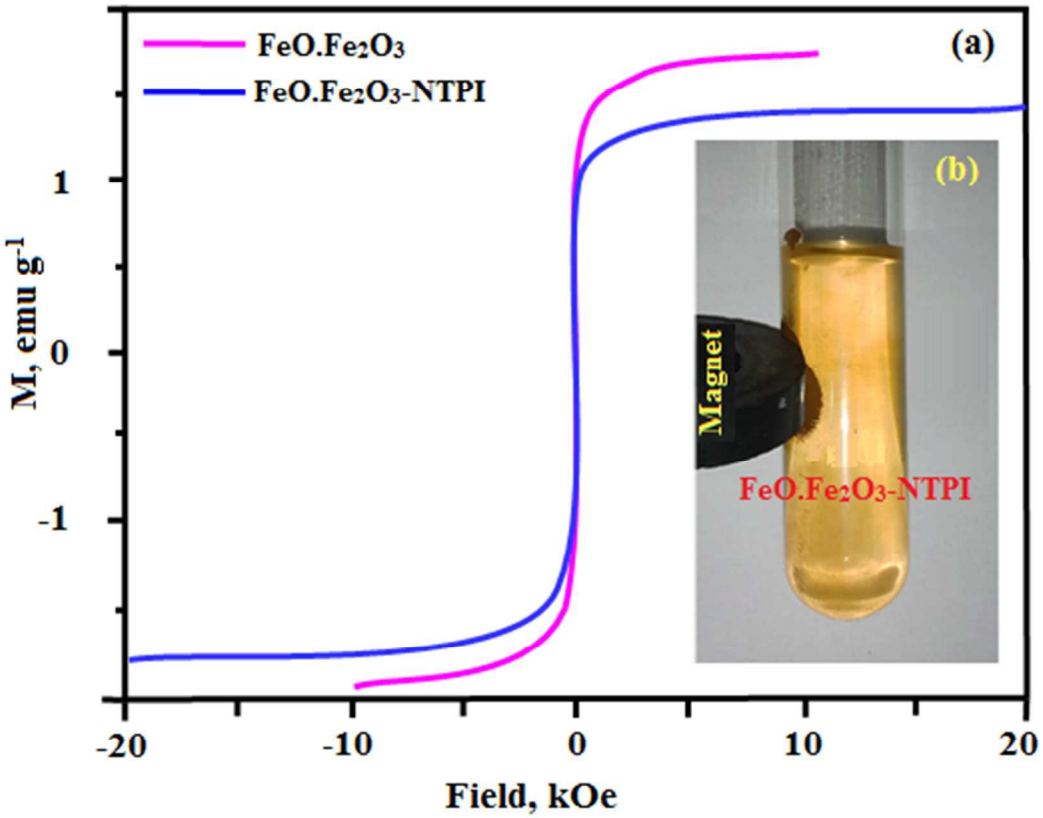

Figure 10

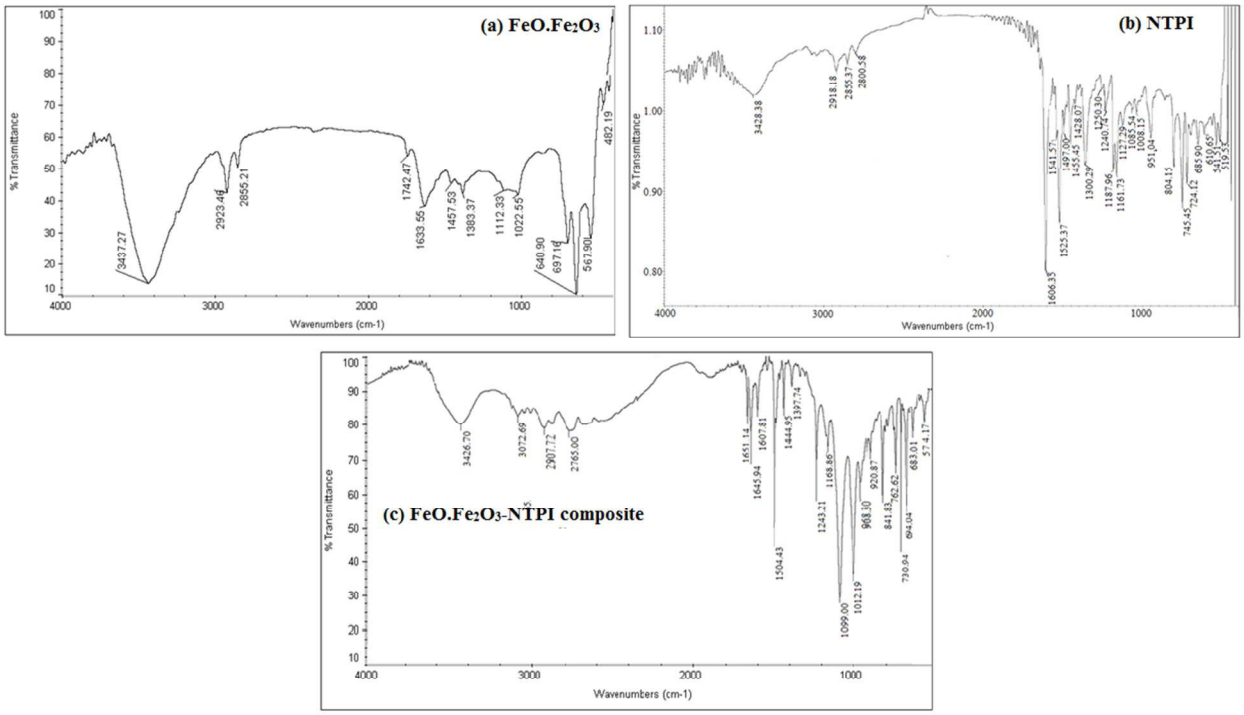

Figure 11

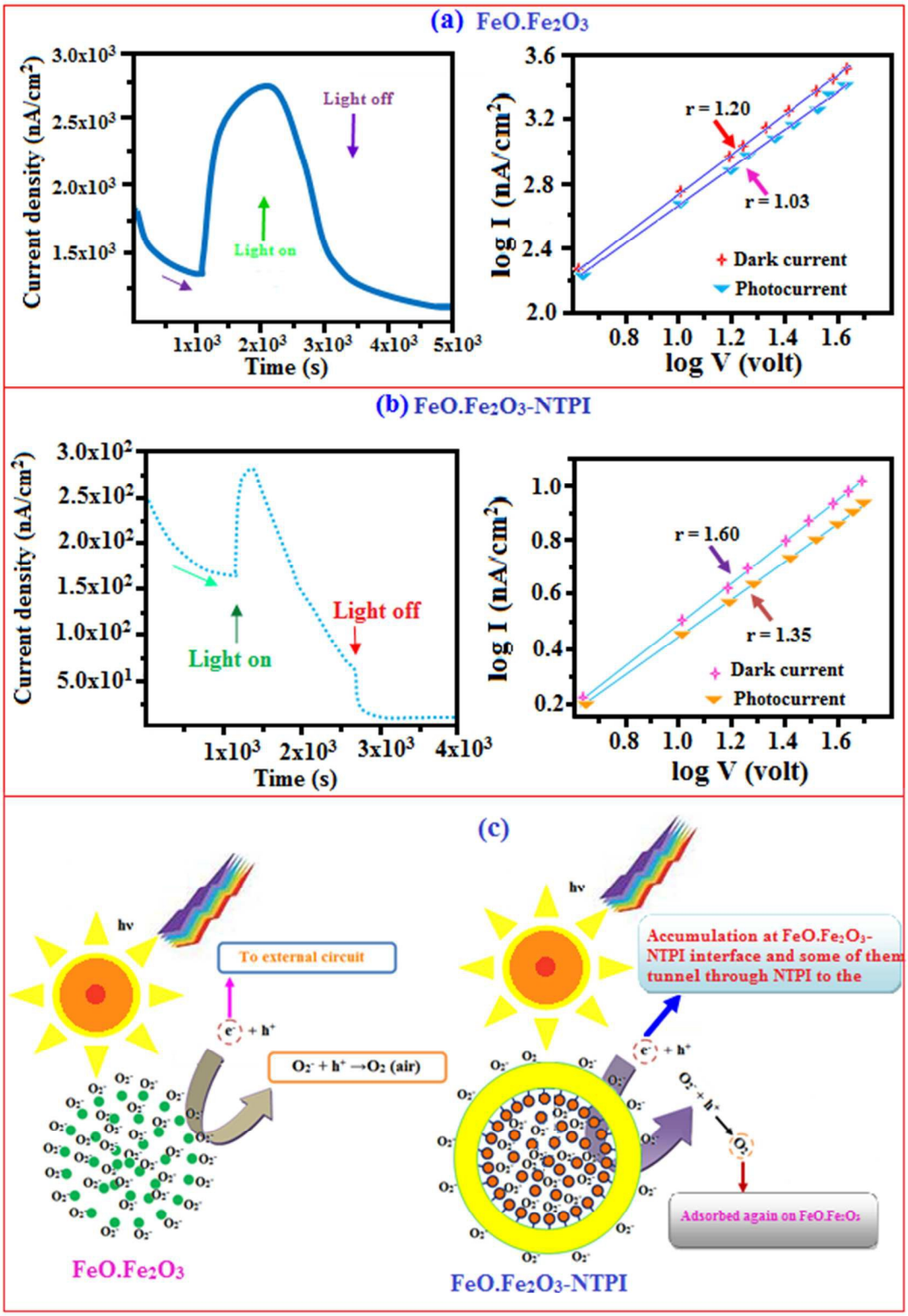

Figure 12

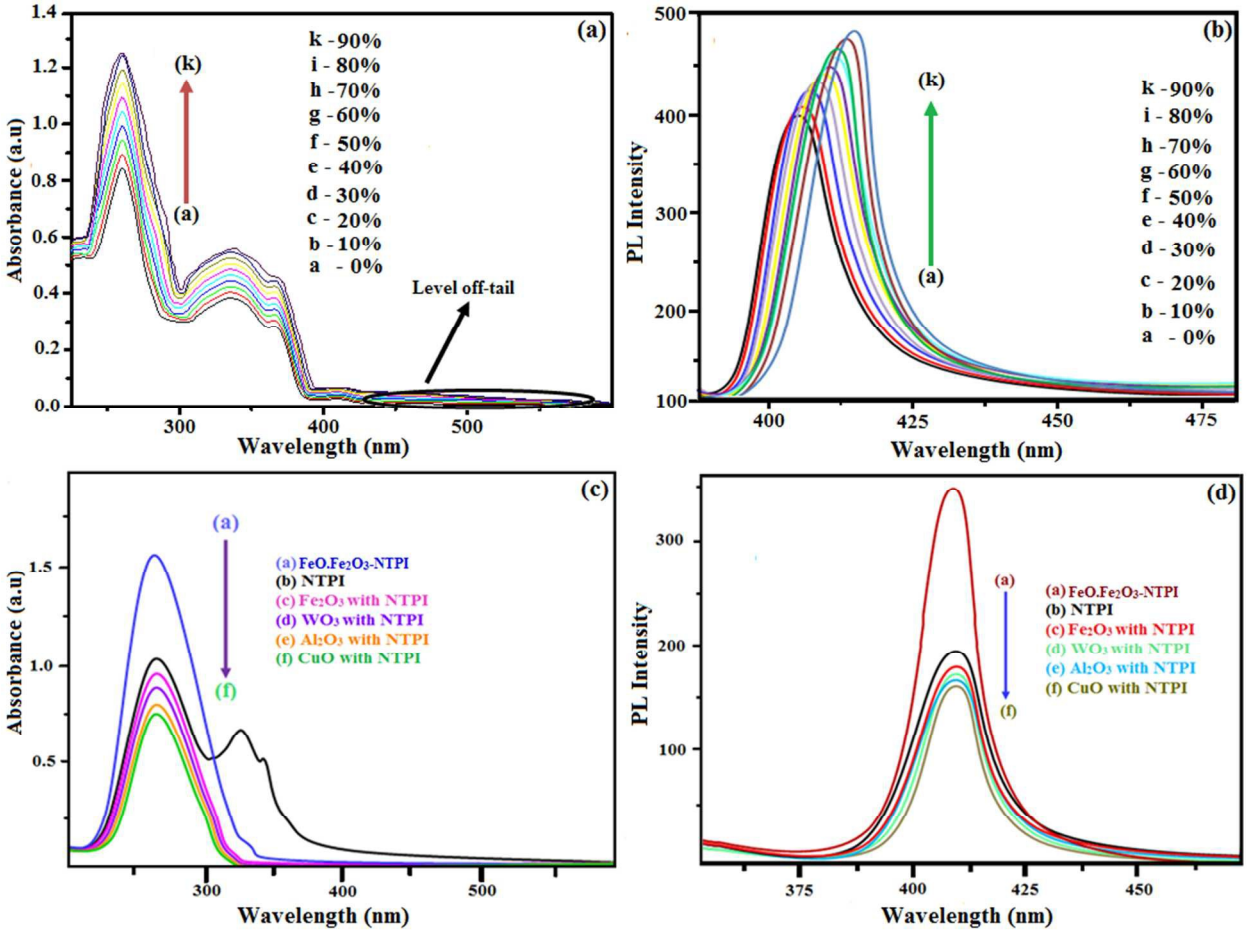

Figure 13

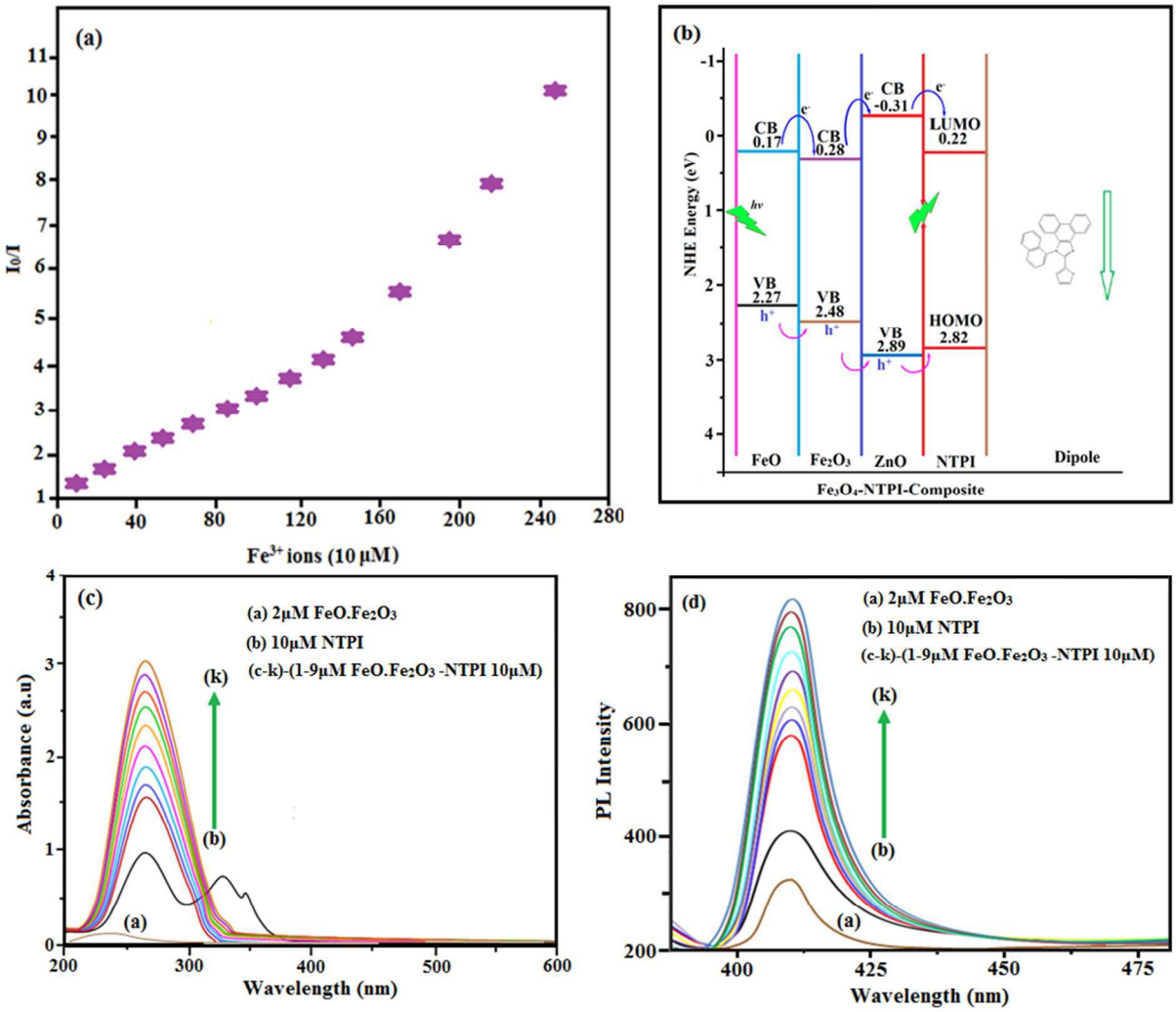

Figure 14

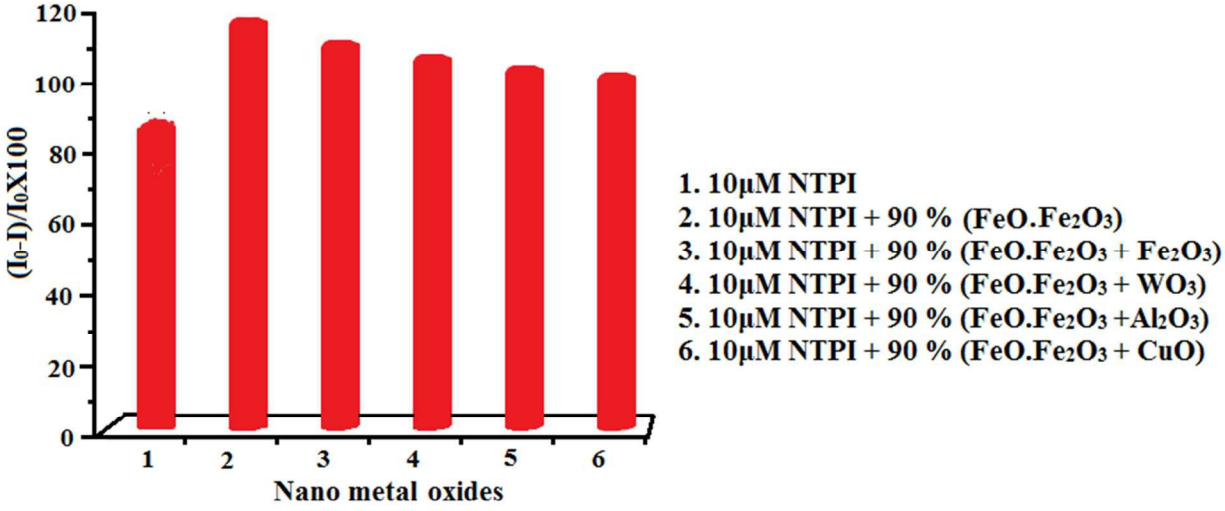

Figure 15

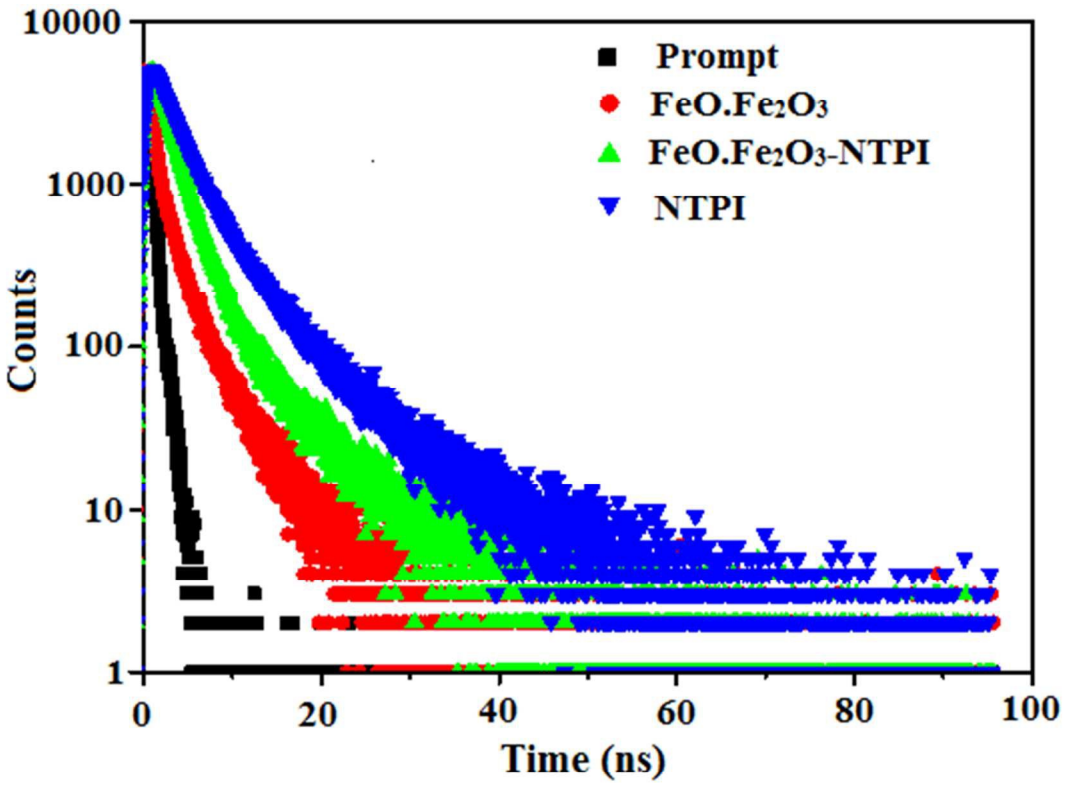

Figure 16

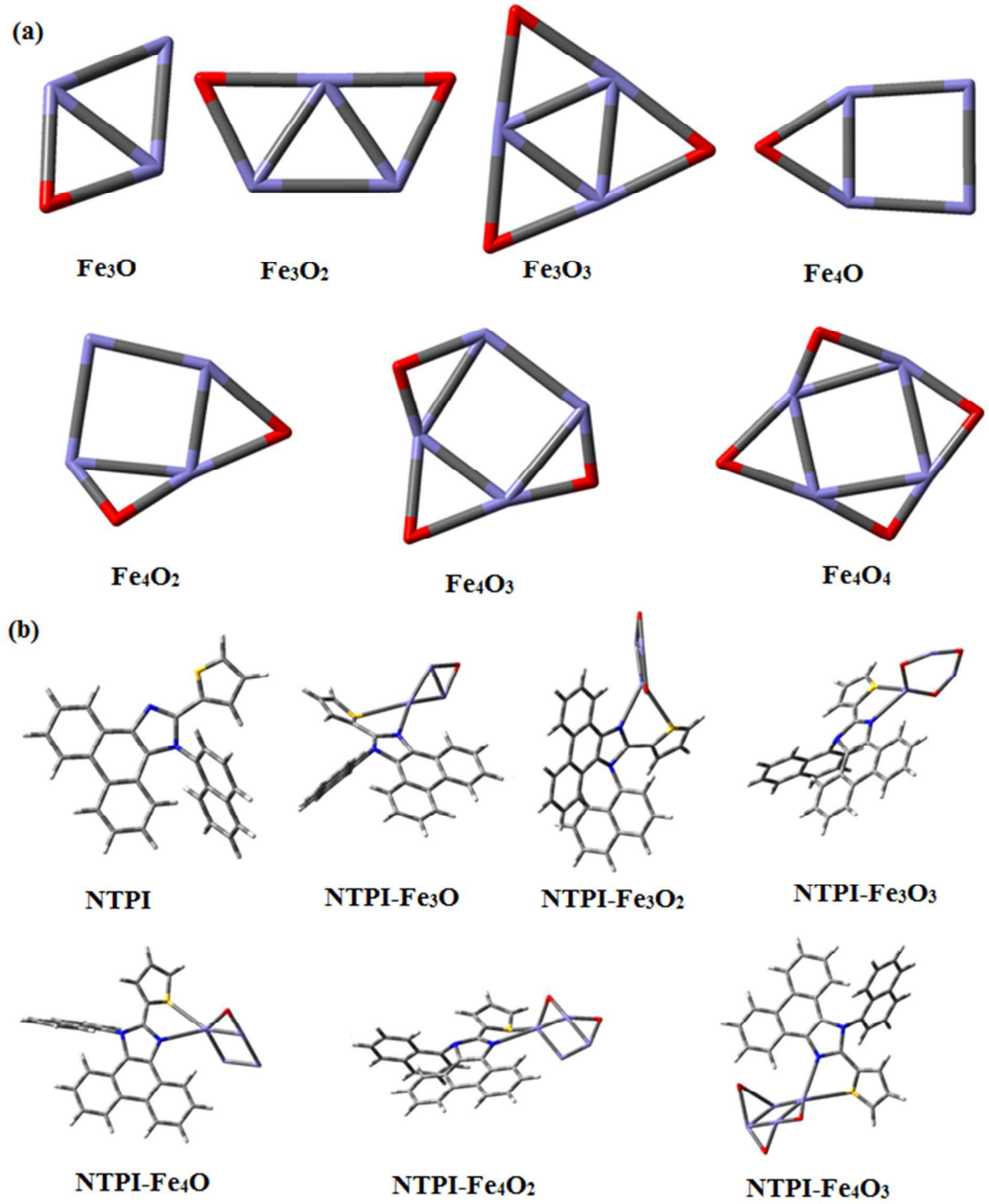

Figure 17

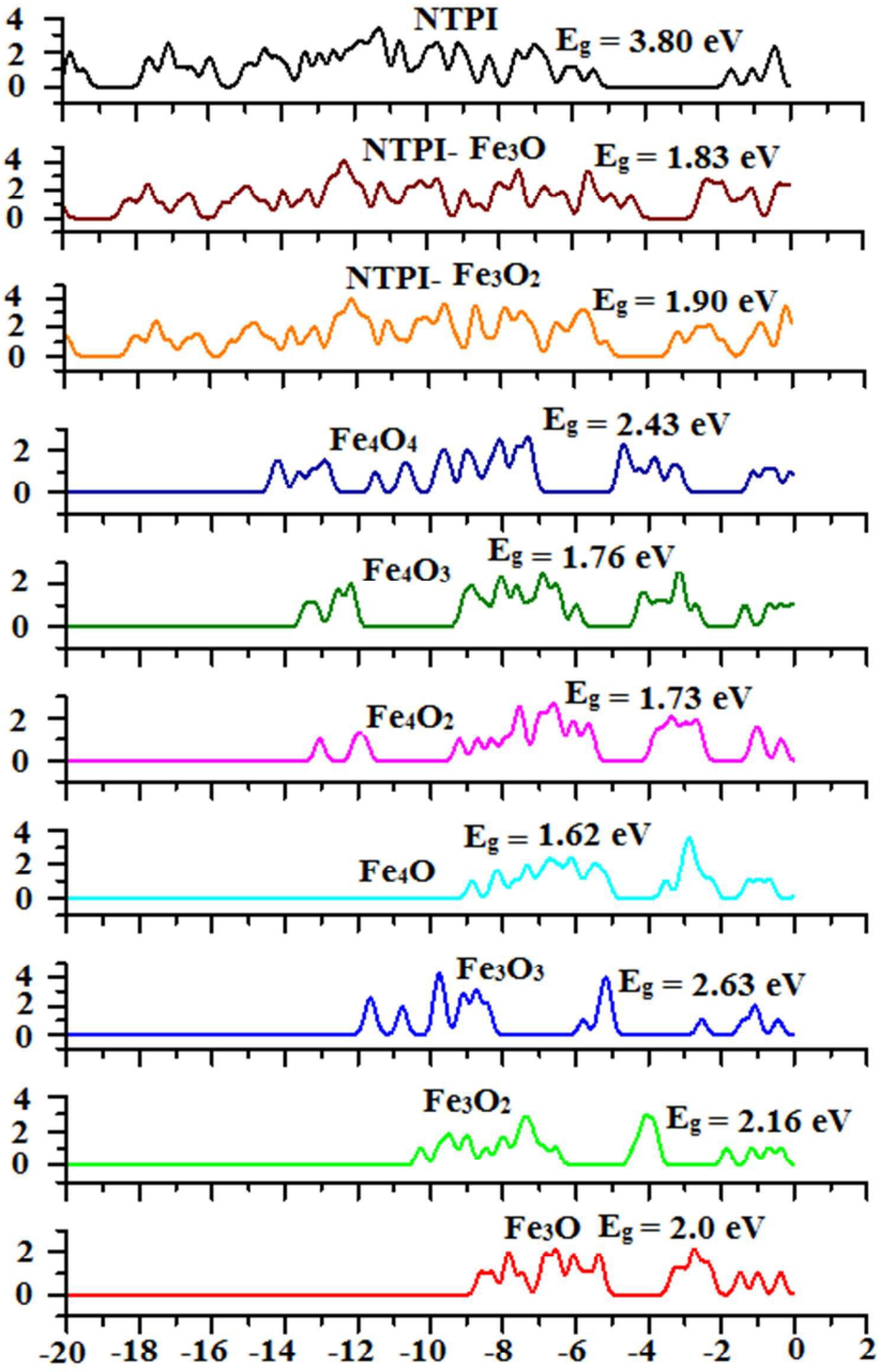

Figure 18

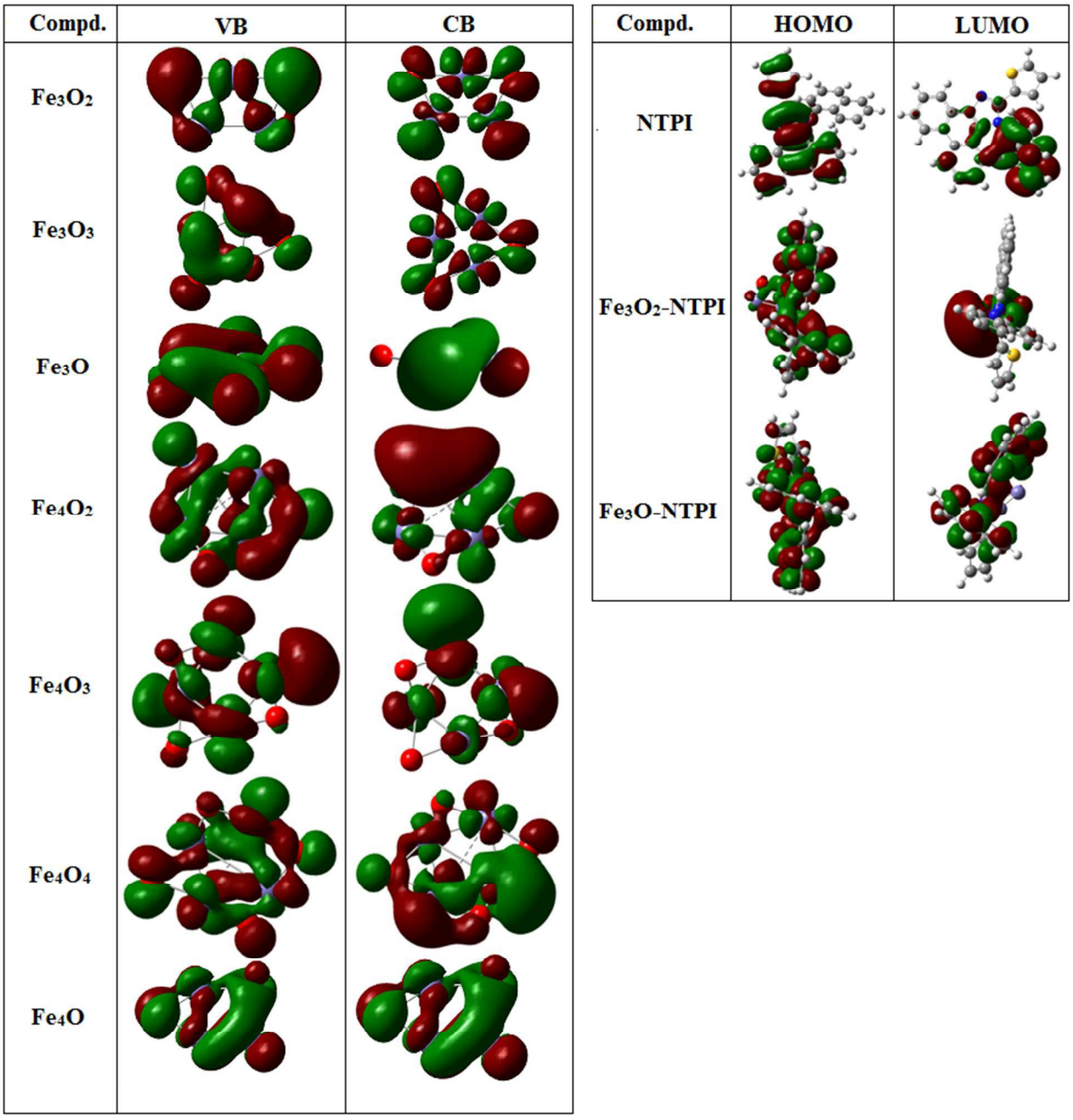

Figure 19

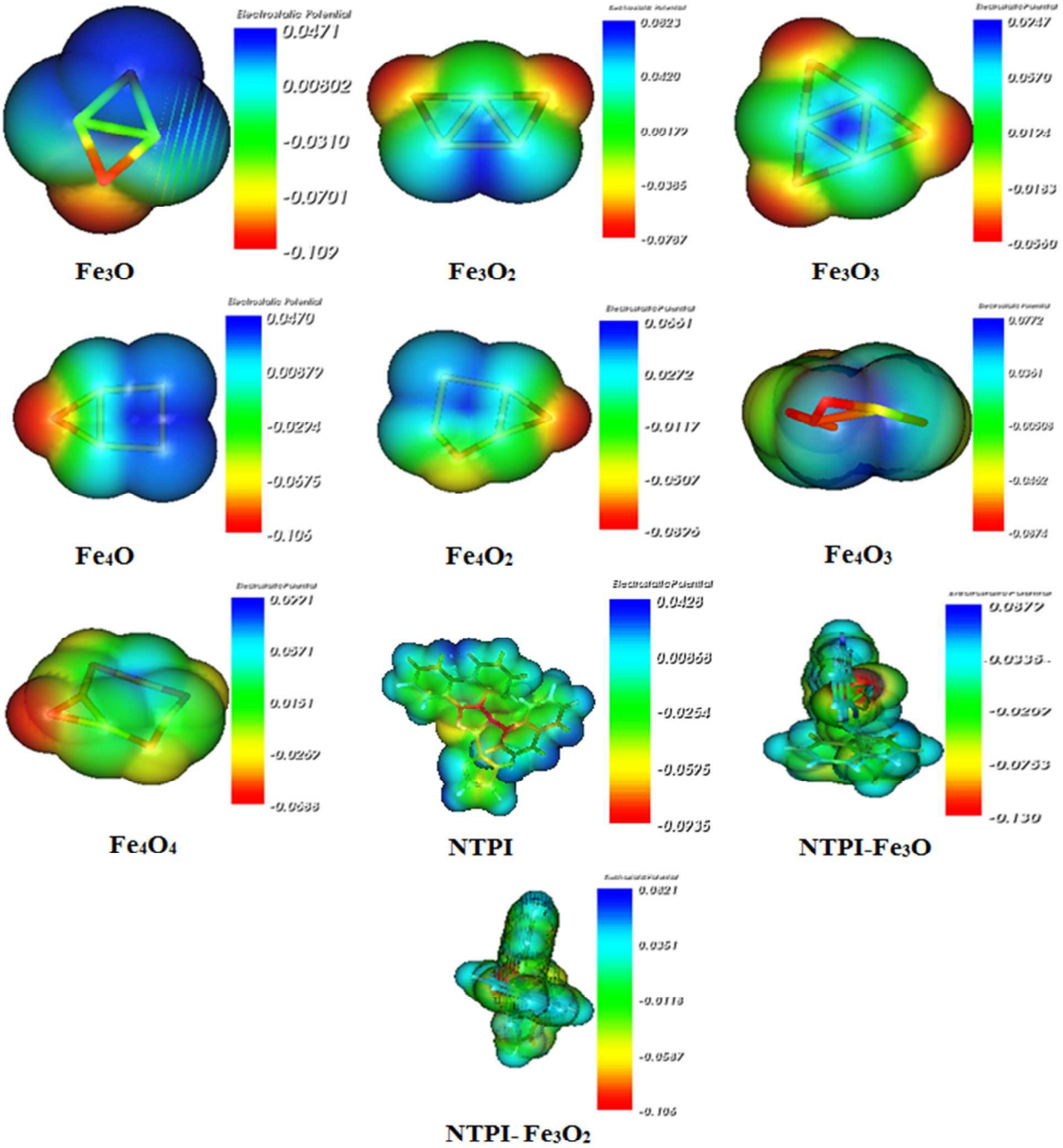

Figure 20

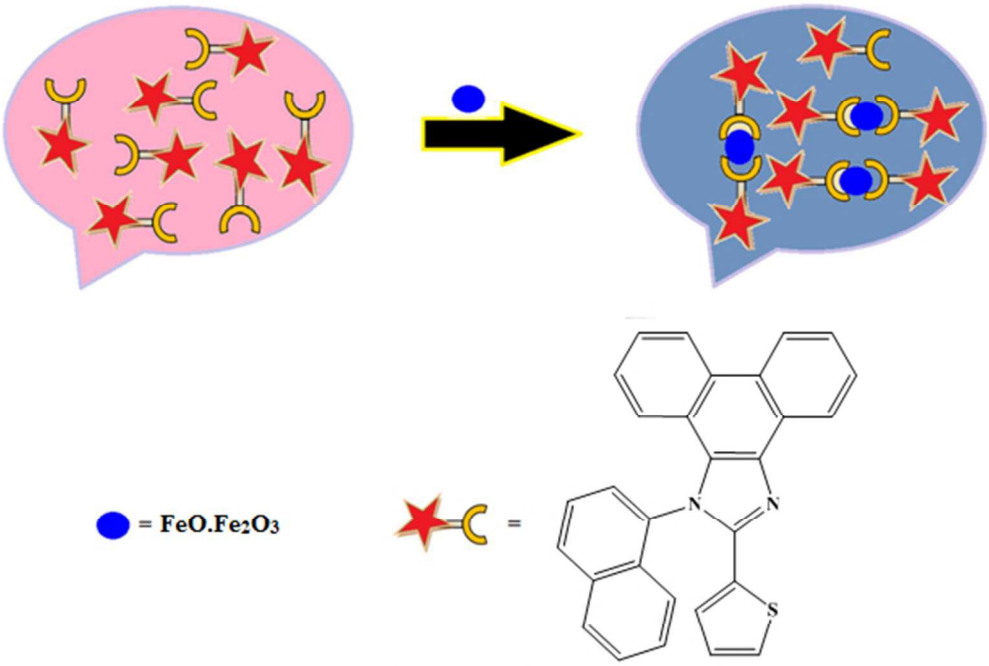

Scheme 1

163x119mm (96 x 96 DPI)

Table 1. Surface properties of pristine $FeO.Fe_2O_3$ and NTPI- $FeO.Fe_2O_3$

Nano Semiconductor	**BET Surface (m^2g^{-1})**	**Total Pore Volume (Single Point) (cm^3g^{-1})**
Pristine Fe_3O_4	23.10	0.10
NTPI-Fe_3O_4	32.82	0.21

Table 2. IR frequencies (cm^{-1}) of NTPI, pristine $FeO.Fe_2O_3$ and $FeO.Fe_2O_3$ -NTPI composite

Bonding	**NTPI**	**Pristine $FeO.Fe_2O_3$**	**$FeO.Fe_2O_3$ -NTPI Composite**
C=N	1606	-	1607
NH str.	3428	-	3426
Aromatic C-C Str.	1541, 1525, 1497, 1455	-	1507, 1444,1397
C-H bending	951, 804, 745, 724	-	958, 920, 841, 762
Fe – O	-	567	574

Table 3. Biexponential fitting parameter for fluorescence decay of NTPI, pristine $FeO.Fe_2O_3$ and $FeO.Fe_2O_3$ -NTPI composite

Compd.	a_1 x 10^{-2}	τ_1 x 10^{-9}	a_2 x 10^{-3}	τ_2 x 10^{-9}	τ_{ave} (ns)	k_r x 10^{-8} s^{-1}	k_{nr} x 10^{-8} s^{-1}	E%	k_{et} x 10^{-10} s^{-1}
NTPI	3.08	2.31	5.52	7.55	5.67	0.10	0.07	-	-
$FeO.Fe_2O_3$ - NTPI	3.82	1.86	1.92	7.13	3.62	0.11	0.16	36.20	9.99
$FeO.Fe_2O_3$	14.80	0.26	5.45	3.15	1.04	-	-	-	-

Table 4. HOMO and LUMO energies (eV), Energy gap (E_g, eV), Fe–N distance (A°), binding energy (E_b, eV), optimised energy (E, eV) and dipolemoments of (μ, D) of NTPI and composites

Compd.	HOMO	LUMO	E_g (E_b) (eV)	E	μ
NTPI	-5.42	-1.62	3.80	6.50	3.4
Fe_3O–NTPI	-4.29	-2.46	1.83 (5.53)	28.60	14.2
Fe_3O_2–NTPI	-5.12	-3.22	1.90 (5.81)	30.08	10.7
Fe_3O_3–NTPI	-5.95	-3.98	1.98 (6.02)	31.58	11.3
Fe_3O	-5.30	-3.30	2.00	12.11	6.23
Fe_3O_2	-6.54	-4.38	2.16	14.16	6.11
Fe_3O_3	-8.41	-5.78	2.63	16.20	0.26
Fe_4O	-5.13	-3.51	1.62	15.47	6.26
Fe_4O_2	-5.56	-3.83	1.73	17.51	7.03
Fe_4O_3	-5.98	-4.22	1.76	19.56	7.45
Fe_4O_4	-7.18	-4.75	2.43	21.61	2.51